Precambrian Research 379 (2022) 106708

Contents lists available at ScienceDirect

Precambrian Research

journal homepage: www.elsevier.com/locate/precamres

Testing the importance of sagduction: insights from the Lewisian Gneiss Complex of northwest Scotland

Sophie R. Miocevich [a], Alex Copley [a], Owen M. Weller [b]

[a] COMET, Department of Earth Sciences, University of Cambridge, Cambridge, UK
[b] Department of Earth Sciences, University of Cambridge, Cambridge, UK

ARTICLE INFO

Keywords:
Archean Tectonics
Metamorphism
Sagduction
Grey Gneiss Terranes
Density Modelling

ABSTRACT

Archean cratons often contain rock units that are interpreted as having been juxtaposed from different structural levels. A range of uniformitarian and non-uniformitarian processes have been invoked to explain these occurrences, prominent amongst which is the density-driven 'sagduction' of high-density upper-crustal lithologies into the underlying dominantly felsic mid-crust. In this paper we test the geological importance of sagduction, using a combination of petrology, phase equilibria modelling, and mechanical modelling. We use the Lewisian Gneiss Complex of northwest Scotland as a test case, analysing the range of observed subordinate felsic–ultramafic bodies within the dominantly felsic crust, but our approach is applicable to Archean terranes globally owing to their analogous lithological ranges. We find that for our thermodynamically-estimated densities of the lithologies present in the Lewisian Gneiss Complex, unrealistically hot temperatures are required for sagduction to be important, given the observed body sizes and available constraints on event durations, geotherms, crustal rheology and emplacement depths. These results suggest sagduction is not responsible for emplacement of the observed subordinate lithologies within the Lewisian felsic mid-crust, and instead support uniformitarian tectonic interpretations. Additionally, our results cast doubt on the importance of sagduction in the structural evolution of granite-greenstone belts. Overall, our study indicates that sagduction was not an important Archean tectonic process.

1. Introduction

Uncertainty surrounds the geodynamic processes operating during the Archean, related to ongoing debates regarding the timing of onset of modern-style plate tectonics (e.g. Korenaga, 2013; Kusky et al., 2018; Cawood et al., 2018; Palin et al., 2020; Windley et al., 2021). As such, both uniformitarian and non-uniformitarian geodynamic processes have been invoked to explain the record of deformation, magmatism, and metamorphism in Archean rocks. These suggestions range from uniformitarian predominantly 'horizontal' tectonic processes, e.g. subduction and modern-style continental deformation (Roman and Arndt, 2020; Garde et al., 2020; Kusky et al., 2021; Nutman et al., 2021; Sotiriou et al., 2022; Weller et al., 2019 and references therein), to a range of non-uniformitarian predominantly 'vertical' processes involving density-driven segregation. The latter include 'sagduction' (also referred to as partial convective overturn), which describes density-driven segregation within the crust (e.g. Collins et al., 1998; Bouhallier et al., 1993; van Kranendonk et al., 2004; Lin et al., 2013; van Kranendonk et al., 2014; François et al., 2014; van Kranendonk et al., 2015; Wiemer et al., 2018; Liu and Wei, 2020; van Kranendonk, 2021), other 'vertical-drip' processes involving delamination of crustal material into the mantle (e.g. Bedard, 2006; Johnson et al., 2014; Sizova et al., 2015; Sizova et al., 2018; Piccolo et al., 2019), and stagnant-lid regime processes, such as heat-pipes (e.g. Moore and Webb, 2013) and mantle overturns (e.g. Bedard, 2018).

Archean terranes, which occur globally, are key in providing insights into what geodynamic processes were operating in the early Earth. Archean rocks vary in appearance depending on the structural level exposed and degree of subsequent reworking. Two main field settings are commonly observed, referred to as granite-greenstone belts and grey gneiss terranes, which can be broadly interpreted as representing the Archean upper crust and mid–lower crust, respectively (Windley and Bridgwater, 1973).

Granite-greenstone belts (e.g. Pilbara, Australia and Barberton, South Africa) are lithologically diverse. The 'greenstones' represent the structurally-highest levels, and typically comprise a range of mafic metavolcanic and metasedimentary rocks that dominantly experienced greenschist- to lower amphibolite-facies conditions (e.g. Anhaeusser, 2014; Furnes et al., 2015; Kusky et al., 2021). The structurally-lower 'granites' range in composition from tonalite-trondhjemite-granodiorite (TTG) to monzogranite and syenogranite, and vary in appearance from massive to foliated (Anhaeusser, 2014 and references

https://doi.org/10.1016/j.precamres.2022.106708
Received 21 December 2021; Accepted 4 May 2022
Available online 5 August 2022

therein). An outcrop style observed in some granite-greenstone belts is a dome-and-basin structure, with granitic domes surrounded by greenstone belts. A variety of processes and numerical models have been invoked to explain this structure, including both modern-style tectonic processes such as fold interference (e.g. Garde et al., 2020; Kusky et al., 2021 and references therein), and density-driven emplacement by sagduction (e.g. Bouhallier et al., 1993; van Kranendonk et al., 2004; Lin et al., 2013; van Kranendonk et al., 2014; François et al., 2014; Johnson et al., 2014; Sizova et al., 2015; Liu and Wei, 2020; van Kranendonk, 2021).

Grey gneiss terranes are thought to represent the mid–lower crustal continuation of granite-greenstone belts, and are dominated by TTG compositions (e.g. the Lewisian Gneiss Complex (LGC), Scotland, and parts of the Superior Craton, Canada; Moyen, 2011; Moyen and Martin, 2012; Percival et al., 2012; Anhaeusser, 2014 and references therein). *P–T* conditions in these grey gneiss terranes typically reached amphibolite- to granulite-facies, consistent with their proposed mid–lower crustal setting (e.g. Feisel et al., 2018; Moyen, 2011; White et al., 2016). The grey-gneiss terranes also contain subordinate lithologies ranging in composition from ultramafic to felsic (e.g. Moyen and Martin, 2012), and in size from meters to kilometres. Owing to the high-grade metamorphic conditions, the protolith of these subordinate lithologies is commonly uncertain, such that it is not possible to discern if the lithologies were emplaced within the TTG host (e.g. as an igneous intrusion) or were transported from higher structural levels. Where transportation from higher structural levels is invoked, similar to granite-greenstone belt evolution, both modern-style and sagduction processes have been suggested (Johnson et al., 2016).

To address the nature of Archean tectonic processes, this study examines whether sagduction is a feasible mechanism to explain the occurrence of rocks from a shallower structural level in the mid–lower crust. In this paper, we use the term sagduction to refer to intra-crustal density-driven sinking processes, but recognise that sagduction is sometimes used to describe material at the base of the crust dripping into the underlying mantle (e.g. Johnson et al., 2014; Sizova et al., 2015; Sizova et al., 2018; Piccolo et al., 2019). Sagduction has been proposed to occur when a higher density layer occurs structurally above a lower density layer. Material from the upper layer sags into the lower layer through the development of a Rayleigh Taylor instability. Continued settling leads to the development of 'droplets' of higher density material sinking into lower density material. Such a scenario has been found to occur in some numerical models of Archean crustal evolution and has been applied to both granite-greenstone belts and grey-gneiss terranes (e.g. Johnson et al., 2014; Sizova et al., 2015; Johnson et al., 2019, and references therein). Previous work has mainly been concentrated on observations from granite-greenstone belts. Here, we instead focus on grey-gneiss terranes, and integrate field and petrological observations, phase equilibria modelling, and a mechanical model of density-driven tectonics to explore under what conditions (e.g. hydration state, pressure–temperature-time conditions, and mineralogy) sagduction is geologically significant. As a test case for this approach, we analyse the Lewisian Gneiss Complex (LGC) of northwest Scotland (Fig. 1a), a classic Archean grey-gneiss terrane where sagduction has previously been proposed (Johnson et al., 2016).

A challenge in performing such work is to accurately assess the importance of sagduction over a range of conditions leading up to the peak metamorphism experienced in poly-metamorphic terranes. In this paper, we achieve this aim by using thermodynamic models to simulate the mineralogy and densities of the relevant lithologies over a wide range of pressure (*P*) and temperature (*T*) conditions, and before and after melt loss. We also consider experimentally-derived estimates of mineral rheology for a range of hydration states and minerals. We are therefore able to ascertain the importance of sagduction during any phase of the geological history of the region.

We initially describe the field setting of the LGC, and the petrology of the TTG gneiss and subordinate lithologies. We then apply phase equilibria modelling to determine both the pressure and temperature conditions experienced by the various lithologies, and how their densities vary over *P–T* space. These results then form the input to a numerical model of sagduction, which in combination with published mineral flow laws allows us to test the physical viability of the emplacement of the subordinate lithologies within the TTG gneiss by this mechanism. Finally, we discuss the implications of our work for Archean tectonics in general, as the lithologies we consider are common to Archean terranes globally.

2. Geological setting

The Lewisian Gneiss Complex (LGC) is located in northwest Scotland (Fig. 1a), and mainly comprises tonalite-trondhjemite-granodiorite (TTG) gneiss, with minor occurrences of other ultramafic to felsic gneiss (e.g. Peach et al., 1907; Sutton and Watson, 1951; Bowes et al., 1964; Cartwright et al., 1985). Protolith ages for the LGC range from 3.1–2.7 Ga, and the complex experienced polyphase metamorphism from ~2.8–1.5 Ga, with *P–T* conditions and timings varying across the LGC, as described below (e.g. Kinny, 1997; Love et al., 2004; Kinny et al., 2005; Love et al., 2010; Macdonald et al., 2015; Fischer et al., 2021).

The regional structure of the LGC remains debated, with the main suggestions being that the LGC is made of up to nine distinct terranes (Kinny et al., 2005), based largely on geochronological data, or that the LGC represents one coherent block of Archean crust, with lateral variations in the timing and conditions of metamorphism due to variations in exposed structural levels (Sheraton et al., 1973; Park and Tarney, 1987; Fischer et al., 2021). The latter hypothesis is gaining traction due to similar peak *P–T* conditions and lithologies being reported across some of the geochronologically-defined terrane boundaries (Feisel et al., 2018).

Previous studies of the LGC have generally focused on the mainland, which is divided into northern, central and southern regions (Fig. 1a) based primarily on metamorphic history, with the northern and southern regions preserving peak amphibolite-facies metamorphic conditions and the central region preserving peak granulite-facies assemblages (e.g. Peach et al., 1907; Sutton and Watson, 1951). The central region is therefore interpreted as representing deeper crustal levels than the rest of the LGC and is the focus of this study.

2.1. Central region of the LGC

Three metamorphic events are distinguished in the central region, which from oldest to youngest are: the granulite-facies 'Badcallian', the amphibolite-facies 'Inverian', and the greenschist- to amphibolite-facies 'Laxfordian'. The Badcallian event generated the highest temperatures experienced by the LGC, and was mainly characterised by peak conditions of 8–10 kbar and 900–1000 °C (e.g. Johnson and White, 2011; Feisel et al., 2018), and led to partial melting of most felsic–mafic lithologies, as evidenced by the occurrence of minor leucosomes and felsic sheets in the region (Johnson et al., 2012; Rollinson, 2012; Johnson et al., 2013). However, most melt is thought to have been lost from the current erosion level, based on widespread depletion in large-ion lithophile elements (Sheraton et al., 1973) and the preservation of granulite-facies assemblages (White and Powell, 2002). The granulite-facies assemblages were partially overprinted during the Inverian at conditions of 3–6 kbar and ~600 °C (Zirkler et al., 2012), with overprinting mainly associated with steeply-dipping northwest–southeast trending shear zones (Attfield, 1987) (Fig. 1b). The duration and continuity of the Badcallian and the Inverian are debated, with geochronological interpretations including that they were two separate events at ~2.8–2.7 Ga and ~2.5–2.4 Ga (e.g. Whitehouse and Kemp, 2010; Goodenough et al., 2013), or a protracted event over a ~200 Myr window (Friend and Kinny, 1995; Taylor et al., 2020). The Inverian event is defined as ending before the emplacement of the 'Scourie Dykes', a

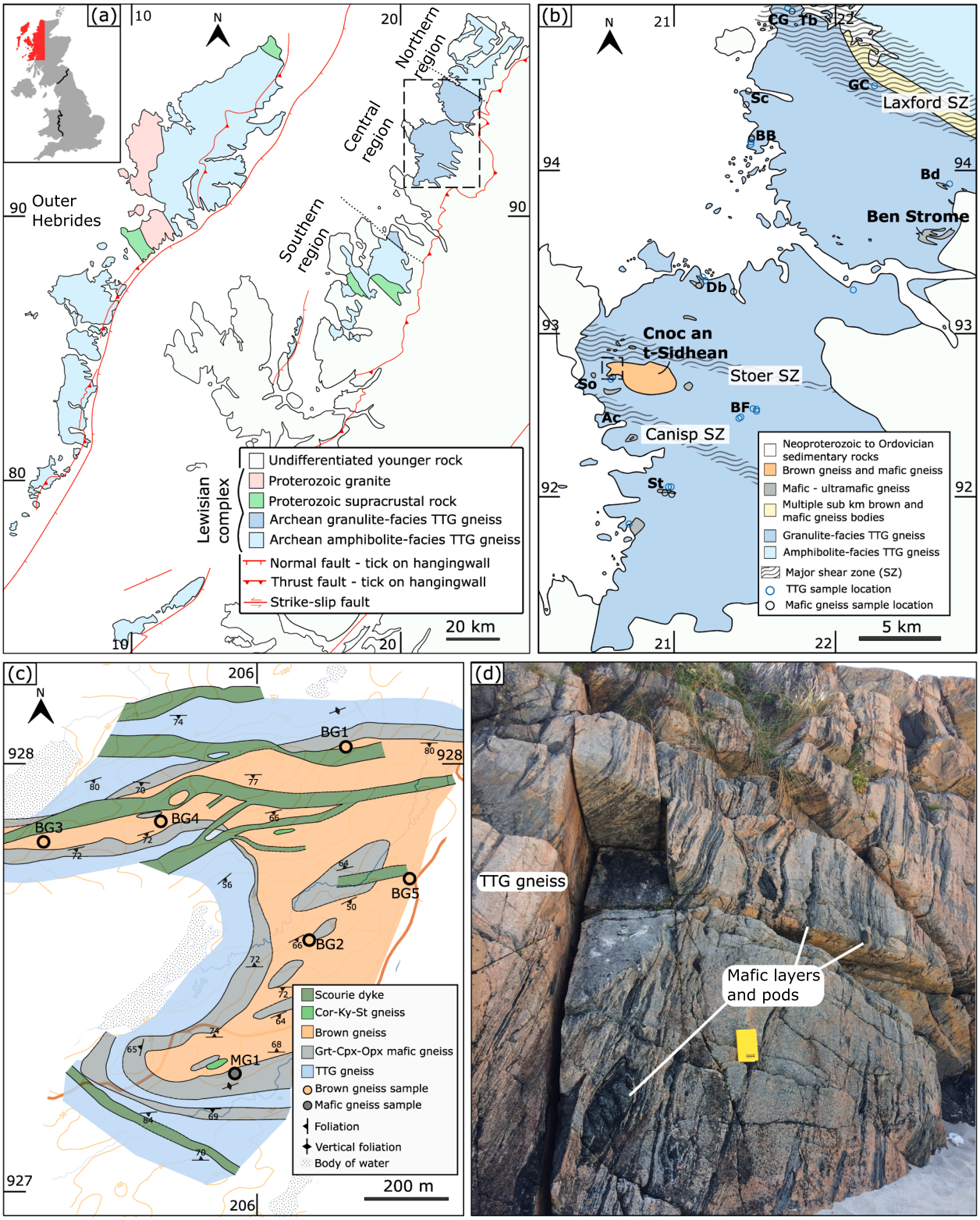

Fig. 1. **(a)** Overview of the LGC. Longitude/latitude ticks are labelled with the first two digits of the British national grid. Dashed box demarcates region shown in (b). The inset shows the location of the map (red region) in the British Isles. **(b)** The distribution of subordinate lithologies in the central region. The largest occurrences of BG-MG (Cnoc an t-Sidhean) and MG-UG (Ben Strome) are labelled. MG and TTG gneiss sample locations outside Cnoc an t-Sidhean and Ben Strome are marked by grey and blue circles. Ac: Achmelvich, BB: Badcall Bay, Bd: Ben Dreavie, BF: Blàr nam Fear Mòra, CG: Cnoc Gorm, Db: Drumbeg, GC: Gorm Chnoc, Sc: Scourie, So: Stoer, St: Strathan, Tb: Tarbet. SZ = shear zone. Dashed box shows region covered by (c). **(c)** Map of the western part of Cnoc an t-Sidhean (based on our fieldwork), with BG and MG sample locations marked. Ticks are labelled with the first three digits of the British national grid. **(d)** Representative central region TTG gneiss at 20588 92523 (near Achmelvich; Ac on (b)) showing 5–20 cm scale layers and boudins of MG within the TTG gneiss. Notebook height = 19 cm.

distinctive suite of northwest–southeast trending mafic–ultramafic dykes that intruded at 2.42–2.38 Ga and are observed to be mostly undeformed by the Inverian (Heaman and Tarney, 1989; Davies and Heaman, 2014). Finally, the central region experienced a series of greenschist- to amphibolite-facies events at 1.9–1.5 Ga, collectively referred to as the Laxfordian. The Laxfordian resulted in widespread retrogression and is associated with the emplacement of granitic pegmatite dykes, and the generation of narrow east–west trending shear zones (Beach, 1973; Goodenough et al., 2013).

The central region is dominated by TTG gneiss, and contains three main subordinate lithologies: biotite-rich gneiss that frequently contains garnet and has been referred to as 'brown gneiss' (BG) in the literature, mafic gneiss (MG) and ultramafic gneiss (UG). These lithologies are described in more detail below (Section 3), and are present as bodies ranging in size from m- to km-scale that are typically lithologically composite in nature (e.g. the body in **Fig. 1c**, which is comprised of BG and MG). A wide range of emplacement levels have been suggested for the protoliths of these bodies, ranging from the near-surface (Park and Tarney, 1987; Sills, 1981; Zirkler et al., 2012; Johnson et al., 2016) to the lower crust (Bowes et al., 1964; Guice et al., 2018a; Guice et al., 2020). Other minor lithologies occurring in the central region, such as Badcallian felsic sheets and Laxfordian pegmatites, are not considered further in this study.

The largest occurrence of subordinate lithologies in the central region of the LGC is the Cnoc an t-Sidhean locality (Fig. 1b), which has a maximum width of 4.4 km and represents the core of a periclinal synform (Cartwright et al., 1985). A map of the western edge of Cnoc an t-Sidhean (Fig. 1c), which is representative of the overall structure and lithologies (Cartwright et al., 1985), shows that it predominantly comprises BG. Mafic gneiss occurs as lenses within the BG and in a 20–100 m layer around the margins of the BG. Rare lenses of muscovite-rich staurolite-kyanite-corundum gneiss also occur within the BG on a ten-metre scale, and Scourie dykes cross-cut all lithologies. Many contacts between lithologies are not exposed, including the bounding contact between the composite subordinate lithologies and the TTG gneiss host. Where contacts are exposed they are typically sharp, occurring over a few centimetres, and sheared. A previous study of Cnoc an t-Sidhean by Zirkler et al., 2012 suggested the region experienced peak *P–T* conditions of 13–16 kbar and $> 900\ ^{\circ}C$. These conditions are higher pressure compared to the rest of the central region (Feisel et al., 2018).

3. Central region lithologies and bulk rock chemistry

Here, we briefly describe the four main lithologies present in the central region: TTG gneiss, brown gneiss (BG), mafic gneiss (MG) and ultramafic gneiss (UG). The lithologies are presented in order of decreasing average SiO_2 content, which is an important factor in controlling their relative densities, as discussed in later Sections. All assemblages represent the metamorphic re-equilibration of the original lithologies.

3.1. Methods

Sixty samples from the LGC are considered in this study (22 TTG gneiss, 5 BG, 15 MG and 18 UG), incorporating published data and our fieldwork (Table S1). Whole-rock data were acquired for all samples, using literature data where available, or measured using X-ray florescence (XRF) at Franklin and Marshall College, Pennsylvania (Table S2). Major element oxides were analysed by fusing 0.4 g of the powdered sample with lithium tetraborate (Boyd and Mertzman, 1987) and $X_{Fe^{3+}}$ was measured by titration. Selected samples were analysed by QEMSCAN (quantitative evaluation of minerals by scanning electron microscopy) to determine mineral modes, using a Quanta650F scanning electron microscope at the University of Cambridge. Mineral compositional data were acquired for sample MG1 (Table S3) using a Cameca SX-100 electron microprobe at the University of Cambridge. Analyses were carried out at 20 keV acceleration voltage and 20 nA probe current, using a 1 μm spot size for garnet and a 5 μm spot size for other minerals. Where given below, all mineral abbreviations follow Whitney and Evans, 2010, and mineral compositional parameters are defined in Table S4.

3.2. Tonalite-trondhjemite-granodiorite gneiss

The TTG gneiss are dominated by quartz and plagioclase and vary in associated mafic phases from clinopyroxene and orthopyroxene to hornblende, biotite, chlorite and epidote (e.g. Fig. 2a,b). The unit commonly exhibits a weak–moderate compositional banding between mafic- and felsic-rich layers, and frequently contains boudinaged mafic to ultramafic layers on a cm- to m-scale (Fig. 1d). Where present, orthopyroxene-bearing assemblages are considered to preserve Badcallian granulite-facies metamorphism (e.g. Rollinson, 2012), whereas pyroxene-absent assemblages are generally considered the product of amphibolite- to greenschist-facies overprinting during Inverian or Laxfordian metamorphism (e.g. Beach, 1973; Sills, 1983). Accessory minerals include apatite, ilmenite, pyrite, rutile and/or zircon. Field observations of quartzo-feldspathic segregations, and microstuctural observations of thin feldspar and quartz films are interpreted as trapped melt pockets (Johnson et al., 2013). The SiO_2 content of 22 TTG gneiss samples from across the central region varies from 54.4–71.3 wt%, with an average value of 65.6 wt%.

3.3. Brown gneiss

The BG typically contains plagioclase, quartz, amphibole and biotite, with garnet variably present (e.g. Fig. 2c,d). The proportions of these phases varies significantly between outcrops, and amphibole and biotite are interpreted as products of retrogression (Cartwright et al., 1985; Zirkler et al., 2012). Apatite, ilmenite, pyrite, rutile and zircon are common accessory phases. The BG commonly exhibit a compositional banding defined by biotite-hornblende-rich and quartz-plagioclase-rich layers. The largest outcrop of BG in the central region is the Cnoc an t-Sidhean locality. Five samples (BG1–5) were collected from this locality to encompass the variation in phase proportions within this lithology (Fig. 1c). Garnet is present in three of the samples (BG1, BG3, BG5) and varies from corroded to euhedral, with larger mm–cm scale porphyroblasts generally showing greater corrosion than mm-scale euhedral garnets. Both varieties of garnet are typically associated with biotite and plagioclase at their margins, with the marginal phases interpreted as retrograde features (Fig. 2c,d). Garnet-absent regions of BG often contain mm–cm scale biotite clots, interpreted as pseudomorphs after garnet. The BG commonly contain leucosomes, which are interpreted as evidence of partial melting (Zirkler et al., 2012). The SiO_2 content of the BG samples varies from 50.4–68.8 wt%, with an average value of 59.7 wt%.

3.4. Mafic gneiss

MG occur throughout the central region, ranging in size from m-scale layers (e.g. Fig. 1d) within the TTG gneiss, to larger decimetre- to km-scale bodies (Fig. 1b), often in association with UG or BG. The MG are generally granoblastic and composed of clinopyroxene and plagioclase, with garnet and orthopyroxene often present (e.g. Fig. 2e,f). Amphibole frequently rims pyroxene and is generally interpreted as a product of retrogression (e.g. Sills, 1983; Johnson et al., 2012). Plagioclase coronas around garnet grains are commonly present, and are also interpreted as retrograde (e.g. Feisel et al., 2018; Johnson et al., 2012). Accessory phases include ilmenite, apatite, sulphides and/or magnetite. Field observations of leucosomes with peritectic phases suggests that the MG experienced dehydration melt reactions. The leucosomes sometimes connect to larger felsic sheets, which are interpreted as evidence of melt transport away from the melt source (Johnson et al., 2012). Fourteen

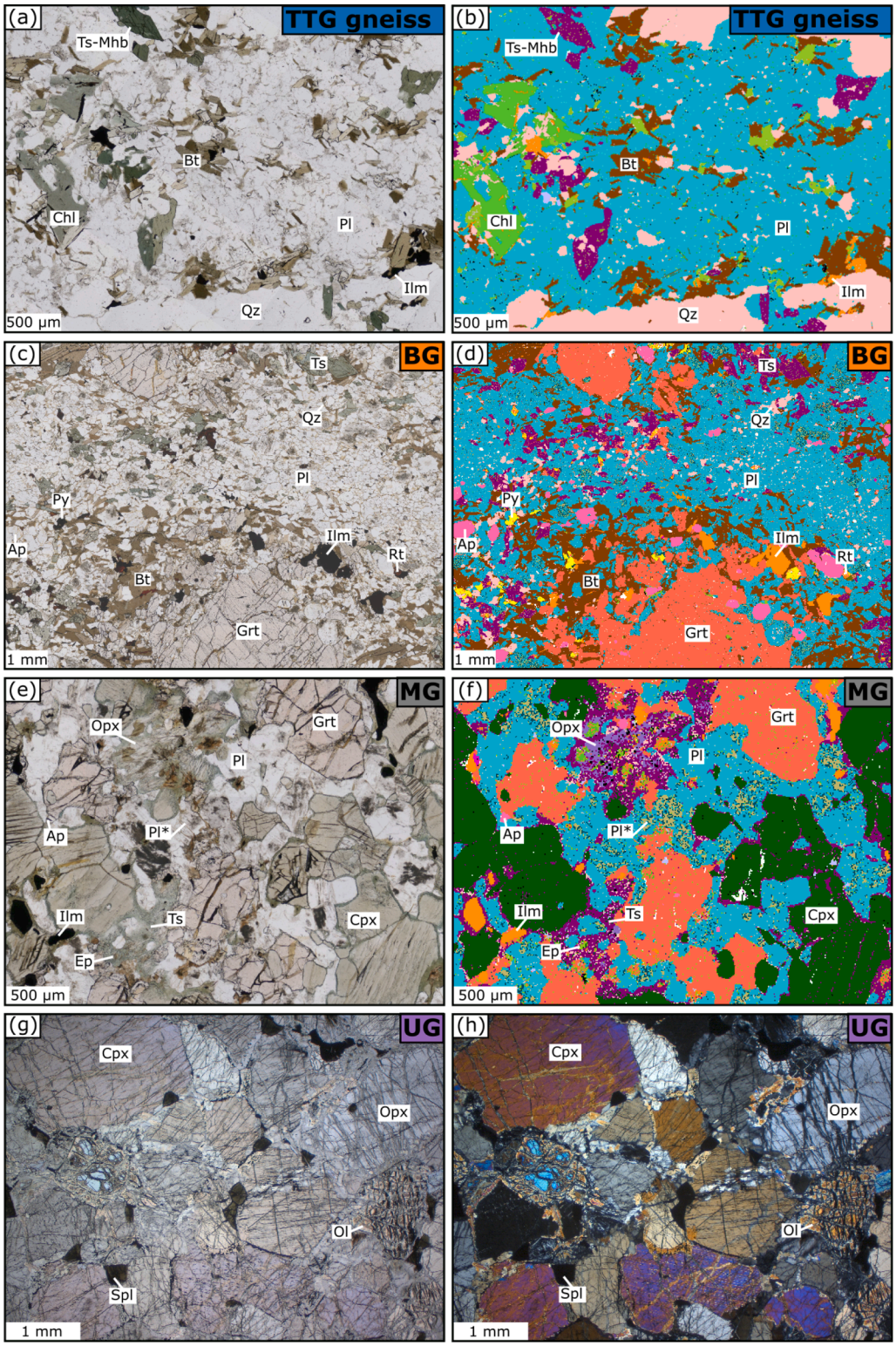

Fig. 2. Petrography of the TTG gneiss (a,b), BG (c,d), MG (e,f) and UG (g,h). Images showing the same field of view for each sample are plane polarised light photomicrographs on the left, and QEMSCAN images (b,d,f) or a cross-polarised light photomicrograph (h) on the right. **(a,b)** TTG gneiss sample from near Achmelvich, exhibiting a greenschist-facies assemblage. **(c,d)** BG sample BG5 from Cnoc an t-Sidhean, showing cm-scale ragged garnet porphyroblasts. **(e,f)** MG sample MG1 from Cnoc an t-Sidhean, showing relict orthopyroxene embayed by amphibole. Pl* is sericitised plagioclase. **(g,h)** UG sample LW16Z11G from Ben Strome (from Guice et al., 2018a), showing a spinel-lherzolite assemblage.

MG samples were used from Feisel et al., 2018, in addition to one sample collected in this study from Cnoc an t-Sidhean (MG1, Fig. 1c; described in detail in Section 4). This sample set covers a range of MG body sizes and compositions. The SiO_2 content of the samples ranges from 43.4–52.8 wt% (average value of 47.8 wt%).

3.5. *Ultramafic gneiss*

The UG typically comprise olivine, orthopyroxene, clinopyroxene and spinel (e.g. Fig. 2g,h), with accessory sulphide phases. Where present, serpentine and amphibole are thought to represent retrogression of olivine and pyroxene, respectively (e.g. Sills, 1982; Guice et al., 2018a). Based on the phase proportions, the UG are generally classified as pyroxenite, with peridotite also present. The UG do not show any evidence

of partial melting. We use whole-rock data of eighteen samples from Ben Strome (Fig. 1b; Guice et al., 2018b), the largest mafic–ultramafic body in the LGC, using those samples classified as least hydrothermally altered. The SiO_2 content of the sample suite ranges from 32.9–44.3 wt% (average value of 39.8 wt.%).

4. *P–T* modelling

Phase equilibria modelling was used to determine the mineralogy and density of each of the four study lithologies (TTG gneiss, BG, MG and UG) over the relevant range of *P–T* conditions (i.e. up to peak conditions), as these parameters will be used in our subsequent numerical models that explore the importance of sagduction. As discussed below, this approach allows us to simulate a range of scenarios for the metamorphic evolution of the LGC, which enables us to account for the evolution of density on the prograde and retrograde path, and effects such as overprinting and melt loss on the present-day mineralogy. The phase equilibria modelling is divided into two sections; in this section we re-evaluate peak *P–T* conditions in the central region, and in the following section we focus on the density and mineralogy of the samples.

Peak *P–T* conditions in the central region need to be revisited because although work by Feisel et al., 2018 yielded consistent peak conditions of 8–10 kbar and 900–1000 °C for 15 MG samples from across the region, a study carried out on a BG sample from Cnoc an t-Sidhean by Zirkler et al., 2012 suggested that this locality experienced significantly higher pressure peak *P–T* conditions of 13–16 kbar (at $>$ 900 °C). This contrast is important for this study because Cnoc an t-Sidhean is the largest body of subordinate lithologies, and the Zirkler et al., 2012 finding implies a much deeper structural level attained than for other bodies of subordinate lithologies. Both body size and depth attained are important for determining sagduction feasibility, as discussed below. To explore this discrepancy, we reassess peak *P–T* conditions at Cnoc an t-Sidhean, using MG sample MG1 from the locality (Fig. 1c).

4.1. Petrography of MG1

Sample MG1 comprises augite (32 vol.%), plagioclase (36 vol.%), garnet (13 vol.%) and amphibole (12 vol.%), with minor orthopyroxene (1 vol.%), ilmenite (2 vol.%), epidote and apatite (Fig. 2e,f). Garnet is Fe rich (X_{alm} = 0.59, X_{grs} = 0.21, X_{prp} = 0.17; Table S3) and unzoned, occurring as 1–2 mm sub-euhedral porphyroblasts with ragged edges. Plagioclase is present as matrix-forming grains, and as rims around garnet, with both forms compositionally indistinct (X_{an} = 0.52), and partially altered to sericite. Augite occurs as anhedral 1–2 mm porphyroblasts and is unzoned with X_{Fe} = 0.39. The augite grains commonly contain exsolution lamellae of orthopyroxene, and have thin rims of tschermakite-magnesiohornblende. Orthopyroxene is also present as optically continuous clusters of sub-mm fragments. These clusters are surrounded and embayed by anhedral amphibole and epidote aggregates, which are therefore interpreted as retrograde. Rare quartzofeldspathic segregations observed in the field are interpreted as leucosomes, from which we infer the presence of a minor melt phase during peak conditions, consistent with Johnson et al., 2012. Overall, MG1 is interpreted to have had a peak assemblage comprising augite, plagioclase, garnet, orthopyroxene, ilmenite and melt.

4.2. Composition and model parameters

Equilibrium phase diagrams (pseudosections) were constructed using Theriak-Domino (de Capitani and Petrakakis, 2010) with dataset ds62 (Holland and Powell, 2011). Calculations were carried out in the Na_2O–CaO–K_2O–FeO-MgO–Al_2O_3–SiO_2–H_2O–Ti_2O–O_2 (NCKFMASHTO) model system using the activity–composition (*a–x*) models considered in Green et al., 2016 (using the high-temperature 'augite' clinopyroxene *a–x* model). Quartz, rutile and H_2O were considered as pure phases. A model bulk composition (Table S5) was calculated for MG1 by adapting the XRF-derived whole-rock data (Table S2), with the aim to best simulate the bulk composition of MG1 at peak conditions. First, based on the observation of (unmodellable) apatite in the sample, the CaO content was reduced by assuming that all of P_2O_5 resided in apatite (Weller et al., 2013). Second, the H_2O content of the sample at peak conditions was approximated by determining what H_2O contents are permissible for the interpreted peak assemblage to be in equilibrium using *T*–M_{H_2O} and *P*–M_{H_2O} pseudosections (Fig. S1). Values of $<$ 0.5 mol.% H_2O meet this criterion, and we use a value at the low end of this range (0.1 mol.%) to minimise the amounts of melt present, in agreement with field observations of cryptic amounts of melt in the region (and by association, the XRF volume analysed). Third, the observation of seriticised plagioclase grains suggests that minor K_2O was added during retrograde metamorphism and hydration. Therefore, K_2O was reduced from 0.4 to 0.2 wt%, to avoid the artificial stabilisation of K-bearing phases. Finally, $X_{Fe^{3+}}$ was set at 0.19, as measured by titration.

4.3. MG1: P–T model results

A *P–T* pseudosection calculated for sample MG1 shows that the interpreted peak assemblage is stable at >875 °C and 8–10 kbar (bold text, Fig. 3a). At lower temperatures amphibole is stabilised, at higher pressures orthopyroxene is absent, and at lower pressures garnet is absent or magnetite joins the assemblage. The coexistence of garnet and orthopyroxene (Fig. 2e,f) provides a relatively well-constrained pressure estimate. To further constrain temperature, contours of garnet vol.% are provided on Fig. 3a, showing that garnet abundance changes rapidly across the peak field, decreasing from ~19 to 0 vol.% as temperature increases. Based on the presence of 13 vol.% garnet in this sample, a maximum temperature of 1000 °C is suggested. The peak temperature was likely to have been lower, as the garnet grains are interpreted to have undergone minor resorption during retrograde metamorphism (Fig. 2e,f), such that the observed garnet vol.% underestimates peak garnet vol.%. Overall, peak *P–T* conditions of 950 ± 50 °C and 9 ± 1 kbar (uncertainties from Powell and Holland, 2008 and Palin et al., 2016) are suggested for sample MG1. Within this range, the proportion of melt is generally ⩽1 vol.%, which is consistent with field observations of minor leucosomes at Cnoc an t-Sidhean.

Our peak *P–T* estimate is consistent with *P–T* estimates from mafic rocks across the central region (Fig. 3b; Feisel et al., 2018), suggesting that Cnoc an t-Sidhean is not anomalous in its tectonic or thermal setting compared to the surroundings. We ascribe the higher pressure result of Zirkler et al., 2012 to the analysis of BG samples, which are more susceptible to retrogression and modification of peak assemblages. Mafic lithologies, as used in this study and Feisel et al., 2018, are considered more reliable for estimating peak *P–T* conditions. As such, based on the modelling here and Feisel et al., 2018's previous results, in the remainder of this paper conditions of 8–10 kbar and 900–1000 °C are taken as peak conditions for the entire central region of the LGC.

5. Density modelling

The purpose of this section is to explore how the assemblages and density of the TTG gneiss and three subordinate lithologies (BG, MG, and UG) vary over *P–T* conditions appropriate to metamorphism of the LGC.

5.1. Model setup

P–T pseudosections and the pixel mapping function in Theriak-Domino (using a pixel size of 10 °C and 0.2 kbar) were used to determine sample mineralogy and density over a range of *P–T* conditions. The model parameters given in Section 4.1 were used for modelling of all TTG gneiss, BG and MG samples. For the UG, pseudosections and pixel maps were constructed in the Na_2O–CaO–K_2O–FeO-MgO–Al_2O_3–SiO_2–O_2–Cr_2O_3 (NCFMASOCr) model system, using the *a–x* models of Jennings and Holland, 2015, as this model system is most

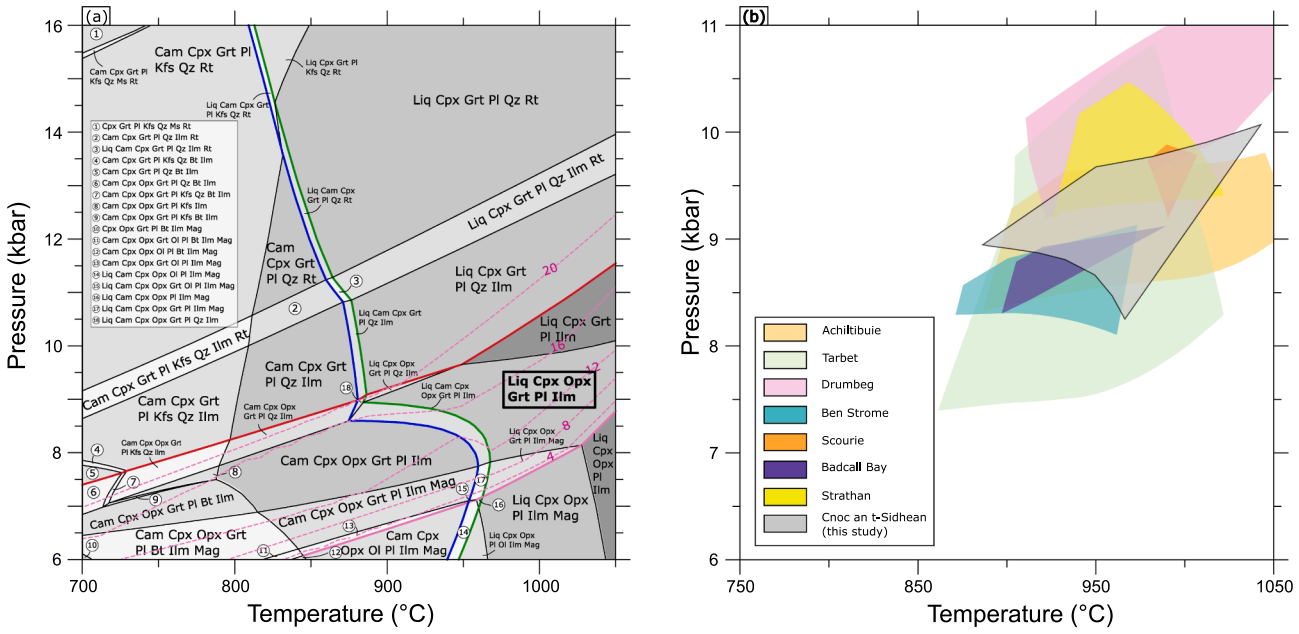

Fig. 3. **(a)** *P–T* pseudosection for Cnoc an t-Sidhean sample MG1, with the peak assemblage highlighted in bold. Zero-mode isolines are provided for garnet (pink), orthopyroxene (red), amphibole (green) and melt (blue). Contours for selected garnet vol.% are shown as dashed pink lines. **(b)** Cnoc an t-Sidhean compared to mafic *P–T* estimates from across the central region (adapted from Feisel et al., 2018).

appropriate for modelling ultramafic lithologies. All model compositions (Table S5, Table S6) were determined by adapting the XRF-derived whole-rock data (Table S2), with the same CaO correction as applied above. For all samples, $X_{Fe^{3+}}$ was set at 0.09, unless measured by titration. For the TTG gneiss, BG, and MG lithologies, modelling was carried out at near anhydrous H_2O contents of 0.1 mol.%, on the basis of the modelling carried out on MG1 above, and to simulate the low water contents typical of granulite-facies terranes. The effects on density of higher water contents (as may have been present during prograde metamorphism), and associated melt loss scenarios, are discussed below. For the UG samples, major element oxides outside the NCFMASOCr model system (e.g. MnO, K_2O, TiO_2 and H_2O) were removed.

5.2. Density estimates

Our main parameter of interest for subsequent modelling is the density difference between the TTG gneiss and each subordinate lithology, as this controls the size of the force driving density-driven sagduction. This parameter requires careful consideration of how factors such as prograde assemblage changes and melt loss could affect the density of each lithology. We initially assess how the density differences vary over a range of *P–T* conditions, using the near-anhydrous model H_2O contents of 0.1 mol.% for the TTG gneiss, BG and MG, and anhydrous model conditions for the UG noted above. Anhydrous conditions are likely a suitable approximation for the prograde to peak evolution of the UG, whereas we acknowledge that the water content for the TTG gneiss, BG and MG is likely only relevant for near-peak *P–T* conditions, following melt extraction. However, the outcome of this modelling is to simulate maximum density differences, based on a discussion below of the evolution of density during prograde metamorphism. This model setup therefore generates maximum density difference end-members that represent the most viable scenarios for sagduction of each subordinate lithology in subsequent sagduction modelling, including during their prograde evolution, which is ideal for the aims of this study.

Fig. 4a–c shows how the density difference between the TTG gneiss and subordinate lithologies varies over *P–T* conditions of 4–12 kbar and 400–1050 °C; conditions that include the peak *P–T* conditions (shown by a shaded box highlighting the range 900–100 °C and 8–10 kbar). The densities used to represent each lithology at each *P–T* condition are obtained by taking an average of the density from all samples of that lithology for each *P–T* pixel. Where *P–T* conditions exceed the liquidus for a given sample, the density can be calculated either including (total density) or excluding (solid density) melt. We initially consider only the solid density, but return to this point below. The plots show that the subordinate lithologies are denser than the TTG gneiss for all considered *P–T* conditions, with the UG and MG denser than the BG. The variation in density difference within each plot (i.e. across the modelled *P–T* range) is small compared to the total magnitude of the calculated density differences between each subordinate lithology and the TTG gneiss, showing bulk composition to have a greater effect than the *P–T* evolution within each compositional category.

For each lithology, example *P–T* pseudosections are included in the supplement, in addition to composite phase diagrams that highlight key phase boundaries for all samples (Fig. S2, Fig. S3). These figures show that the *P–T* conditions considered on the density maps in Fig. 4a–c often exceed the calculated liquidus position for the TTG gneiss, BG and MG samples. Therefore, to evaluate the impact of melt on calculated density, we consider the solid versus total density in the *P–T* window that represents calculated peak conditions (where the largest predicted volume of melt is present at *P–T* conditions relevant to the LGC central region). This calculation is not carried out for the UG lithology, as peak conditions are sub-solidus for all samples. On Fig. 4d, each point represents the difference between the solid density and the total (solid plus melt) density for each sample, averaged over all pixels in the peak *P–T* range. Fig. 4d highlights that the density difference between total and solid density is minimal, varying from 0–0.012 g cm^{-3}. This value is small compared to the difference in density between lithologies (0.10–0.60 g cm^{-3}; Fig. 4a–c), because average melt content never exceeds 2.5 vol.%.

The small melt volumes calculated here are due to the samples being modelled as near anhydrous, based on field and geochemical observations outlined in Section 2.1 and modelling of MG1 in Section 4.2. It is therefore necessary to consider how density would vary at larger melt fractions, as the TTG gneiss, BG and MG lithologies could have experienced melt loss during their prograde history, with the exact details dependent on a range of factors including the *P–T* path, protolith water content and melt loss thresholds. A range of scenarios could be

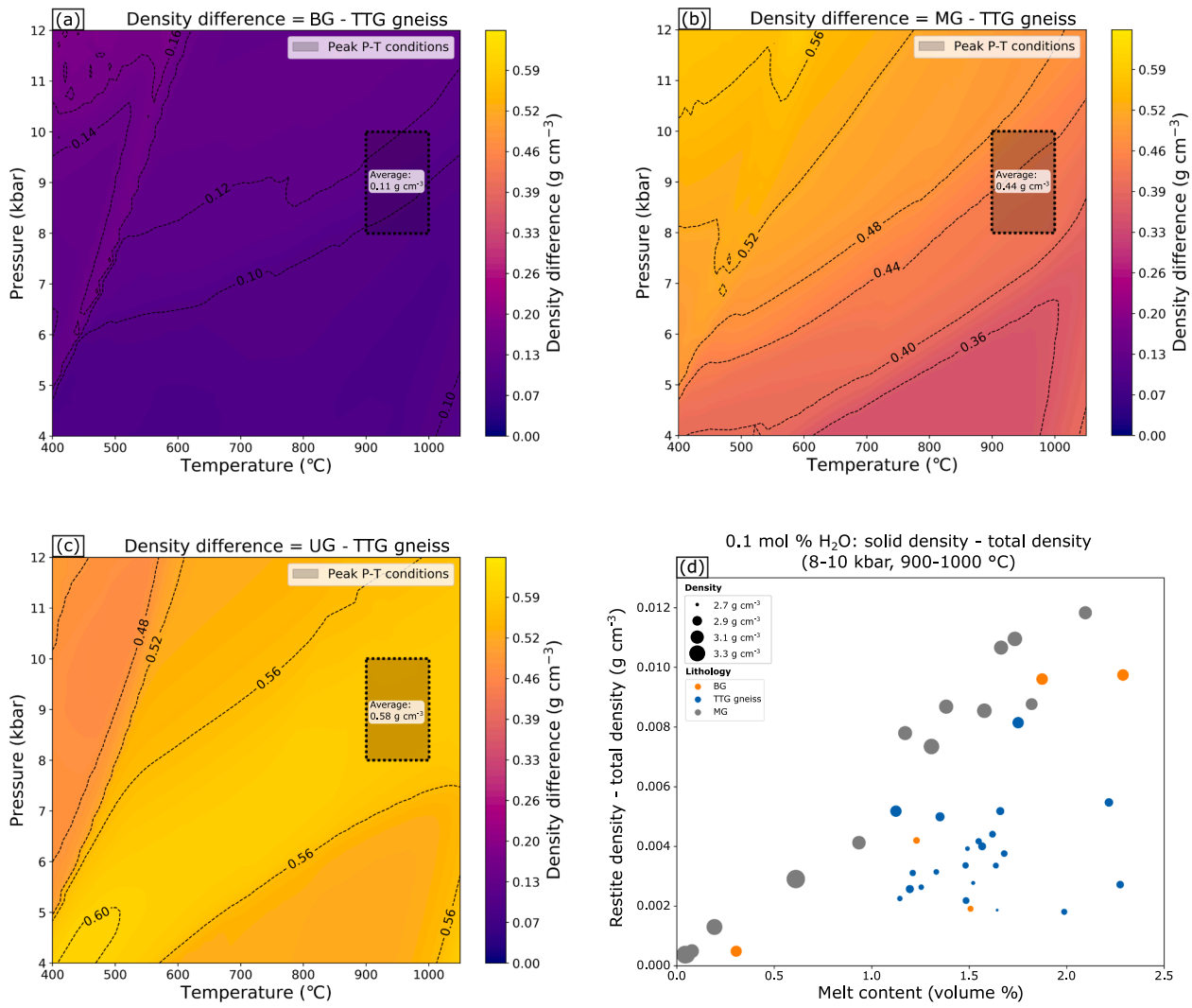

Fig. 4. **(a–c)** Evolution of density difference between modelled lithologies through *P–T* space. Peak *P–T* conditions are shown by the shaded grey box. **(a)** Density contrast between BG average and TTG gneiss average. **(b)** Density contrast between MG average and TTG gneiss average. **(c)** Density contrast between UG average and TTG gneiss average. **(d)** Contrasts between the solid and total (solid plus melt) densities estimated for each sample, with the size of the symbol indicating the density at peak conditions.

simulated, but here we only consider the overall impact of melt loss on density for each protolith, as this approach is sufficient for our purposes. Fig. 4d shows that the density of the TTG gneiss (blue circles) does not markedly vary when melt is removed as the melt and solid have similar (granitoid) compositions (i.e. removing a granitic melt from a rock with granitic bulk composition will not markedly alter the density of the granitic rock). Therefore, TTG gneiss density is unlikely to vary significantly from that calculated, regardless of the details of prograde melt loss history. In contrast, as illustrated on Fig. 4d, the BG and MG lithologies show a correlation between increasing melt loss and increasing density, due to these lithologies having a greater density than the removed melt. As such, if melt removal occurred during prograde metamorphism, these lithologies would have had lower densities before melting occurred, more similar to the TTG gneiss, though always retaining a higher density than the TTG gneiss owing to their increased proportion of ferromagnesian minerals. The density differences for the solid case on Fig. 4a–b therefore represent a maximum density difference between the lithologies, regardless of prograde/melt loss history, and therefore represents the most viable situation for sagduction to be an important process. The UG does not experience melting during prograde metamorphism, so is well represented by Fig. 4c. The UG-TTG gneiss scenario also represents the maximum density difference between the TTG gneiss and subordinate lithologies (up to 0.6 g cm^{-3}).

To further explore the controls on the estimated densities, and because the minerals present control the rheologies (and thus mineral flow laws) to consider in the following models of sagduction, we here analyse the mineralogy of all samples, using sample mineralogy in the peak *P–T* window as a means of comparison (Fig. 5a–b, Table S7). Each point on Fig. 5a represents the vol.% of a given mineral in one sample, averaged over all pixels in the peak *P–T* range, with the symbol size scaled according to the solid rock density of that sample. Fig. 5b averages these modal data to determine the average mineralogy of each lithology at peak conditions. TTG gneiss are predominantly feldspar (61.8 vol.%) and quartz (24.8 vol.%), with minor orthopyroxene, garnet and clinopyroxene; BG are predominantly feldspar (62.7 vol.%); MG are predominantly feldspar (40.3 vol.%) and pyroxene (41.1 vol.%); UG are mainly composed of olivine (50.9 vol.%) and pyroxene (40.1 vol.%).

The solid density of each sample in the peak *P–T* window is plotted against SiO_2 wt% in Fig. 5c. TTG gneiss and BG show overlapping calculated densities due to having similar peak assemblages, dominated by feldspar and quartz with variable orthopyroxene, clinopyroxene, garnet and minor phases (ilmenite, melt). However, BG is generally denser, having higher garnet proportions than TG, and reduced quartz. Compared to the TTG gneiss and BG, MG are higher density, having

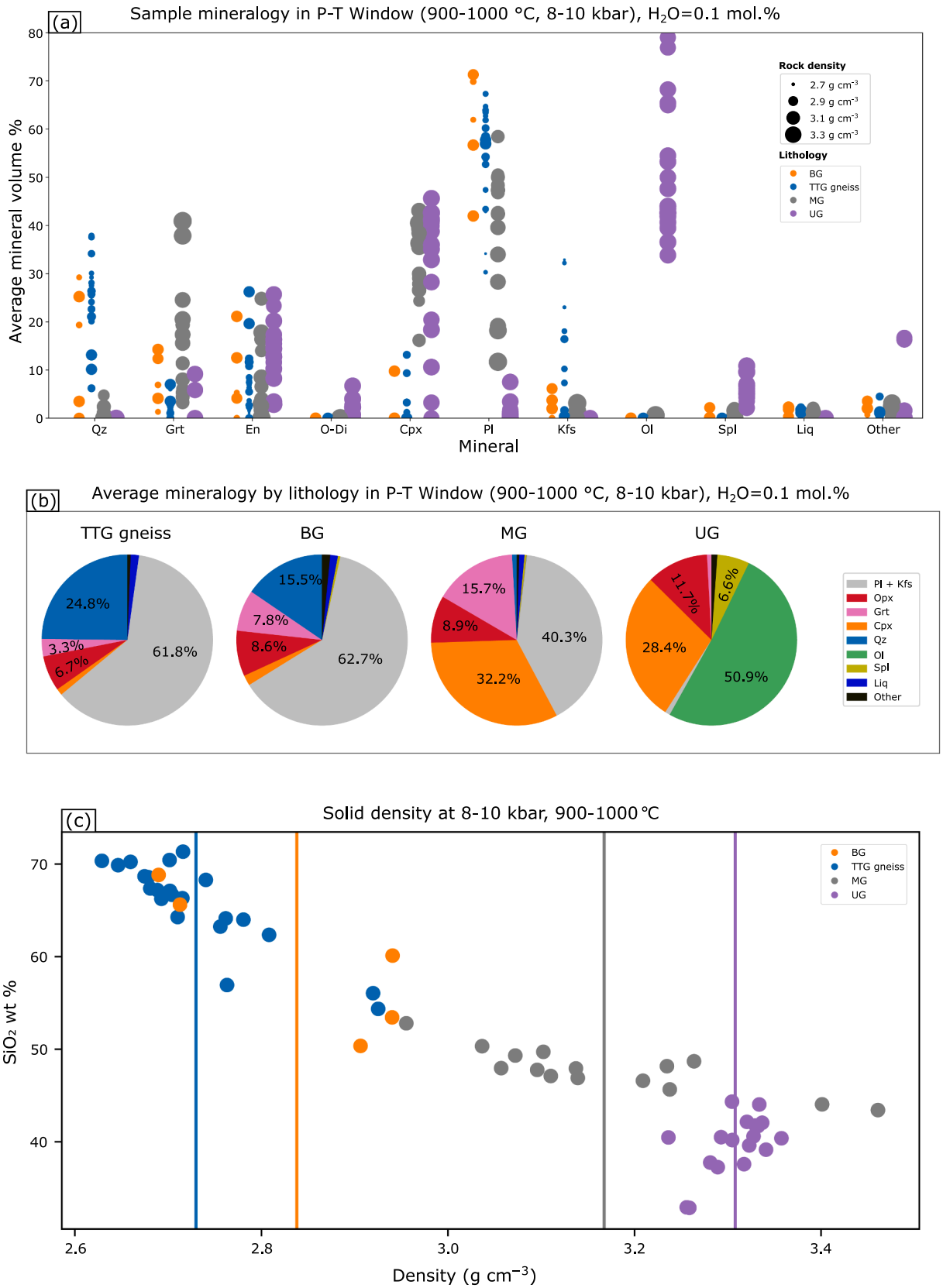

Fig. 5. **(a)** Sample mineralogy in the peak *P–T* window. Each dot represents the vol.% of a given mineral in one sample, with dot colour showing sample lithology. Sample dot size is scaled by density of each sample in the peak *P–T* window. **(b)** Average mineralogy in peak *P–T* window for each lithology. **(c)** Density of each modelled sample at the peak *P–T* conditions. The coloured lines show the averages for each lithology.

markedly higher clinopyroxene and garnet contents and reduced plagioclase. The highest density MG points are due to these samples having particularly high garnet contents. UG have comparable pyroxene contents to the MG and are dominated by olivine, with the absence of low-density feldspar leading to generally higher densities than the other lithologies. These mineralogical contrasts therefore give rise to the density variations shown in Fig. 4a–c.

In the peak *P–T* window, TTG gneiss have an average density of 2.73 g cm^{-3}, BG 2.84 g cm^{-3}, MG 3.17 g cm^{-3} and UG 3.31 g cm^{-3} (vertical lines on Fig. 5c). In order to explore the geological importance of sagduction, we use the density differences between the TTG gneiss and the subordinate, denser, lithologies in subsequent modelling. As discussed above, these density contrasts are a maximum that are likely to have been attained during the metamorphic evolution of the samples. By using these values in the modelling below, we are therefore investigating the importance of sagduction under the most favourable circumstances in terms of density contrast.

6. Sagduction model

6.1. Model setup

Having obtained estimates of the density and mineralogy of all relevant lithologies in the LGC, we now use this information to assess sagduction viability. Sagduction is thought to occur if there is a higher density layer on top of a lower density layer (e.g Collins et al., 1998; Lin et al., 2013). In this situation, the interface between the layers will develop Rayleigh Taylor Instabilities, with small irregularities at the boundary developing into downwelling fluid spikes (e.g. Elgowainy and Ashgriz, 1997; Sharp, 1984). Whether sagduction is geologically important depends upon the rate at which downwelling occurs. To address whether the densities we have calculated imply this process is geologically important, we examine the motion of a spherical droplet that has detached from a downwelling fluid spike (as shown in Fig. 6). This motion is the fastest velocity that a falling droplet can attain, so the model is developed to assess the effectiveness of sagduction under the most favourable possible circumstances. Downwelling spikes still connected to the overlying higher-density layer will have lower sinking velocities (Eggers and Villermaux, 2008).

In such a model, the sinking droplet represents the higher-density subordinate lithologies within the surrounding TTG gneiss. Both the droplet and the TTG gneiss are assumed to be homogenous. We assume the falling droplet is spherical, which is reasonable given the outcrop patterns of the subordinate lithologies, and that Moreau et al., 1981 show that it is acceptable to approximate the radius of near-spherical droplets with an effective radius for a sphere of the same volume. Sagduction is sometimes envisaged as being the downwelling of a coherent diapir of more-dense material. However, provided that the viscosity of the downwelling material is greater than that of the (hotter and less mafic) surroundings, the rate of downwelling will be slower than that of a falling droplet, due to the viscous forces being transmitted through the downwelling fluid spike (Eggers and Villermaux, 2008). Additionally, the outcrop patterns and deformation fabrics of the subrodinate lithologies within the LGC do not suggest that these lithologies were connected to large-scale downwelling fluid spikes (e.g. Cartwright et al., 1985; Zirkler et al., 2012; Guice et al., 2020). Our model setup therefore represents the configuration in which sagduction is most likely to be important, and also that most likely to be applicable to the LGC.

Additionally, we assume the droplet is a rigid body falling through a fluid. It is likely that a droplet undergoing sagduction is also able to deform viscously (and this is in fact required for the initial development of the falling droplet from a Rayleigh Taylor instability). However, we make this approximation to reduce the number of free parameters in the model, and because the behaviour of a deformable droplet with a sufficiently large viscosity contrast with the surroundings approximates that of a rigid droplet (Taylor and Acrivos, 1964). For example, the

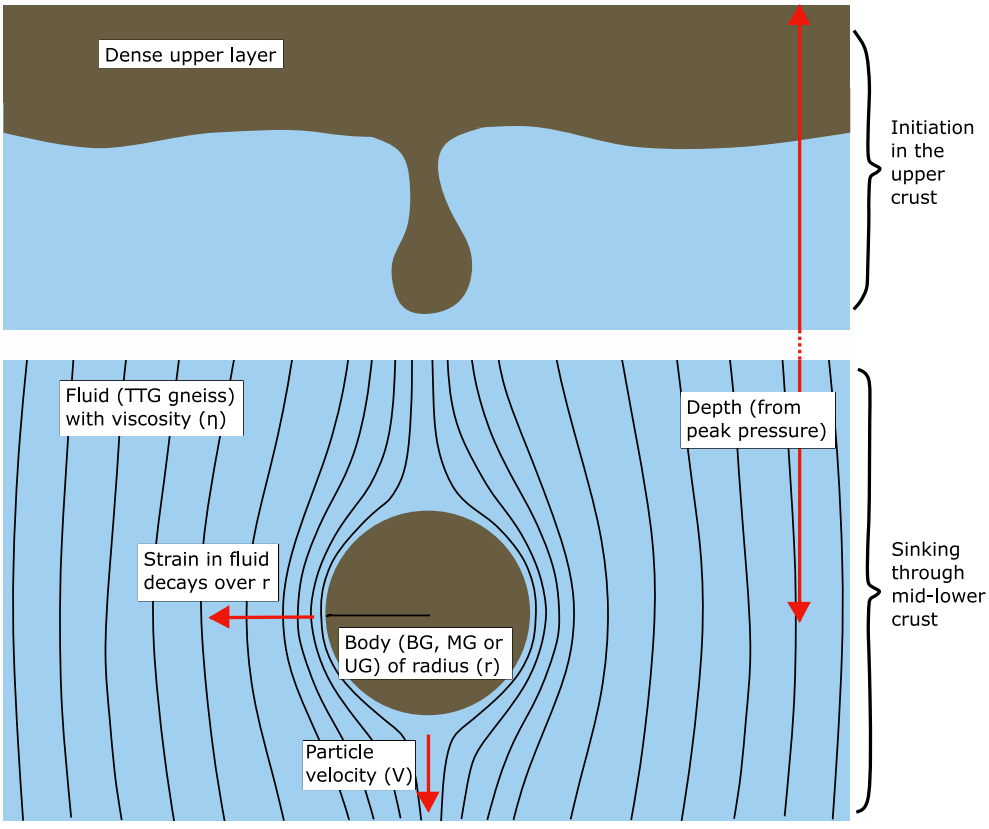

Fig. 6. Summary of sagduction model setup and input parameters. Schematic flow lines are shown, ignoring interaction with the surface layer.

contrast in creep viscosities between feldspars and mafic minerals, which is equivalent to the viscosity contrast between TTG gneiss and the more mafic subordinate lithologies, is likely to be greater than an order of magnitude at crustal conditions (Dimanov and Dresen, 2005; Burgmann and Dresen, 2008; Shinevar et al., 2015). A deformable droplet with a viscosity an order of magnitude greater than the surroundings sinks with a velocity within 5% of a fully rigid droplet, reducing to within 1.5% for a viscosity contrast of a factor of 20, and 0.3% for a factor of 100 (de Villeneuve et al., 2006). These lines of reasoning imply that the assumption of a rigid droplet is justified.

Under these assumptions, and the model setup shown in Fig. 6, Stokes' law can be used to describe the behaviour of the sinking droplet, with the sinking velocity (v) being given by

$$v = \frac{2}{9}\frac{\Delta\rho}{\eta}gr^2 \quad (1)$$

where $\Delta\rho$ is the density difference between droplet and fluid, r is the droplet radius, η is the fluid viscosity, and g is the acceleration due to gravity (Kim and Karrila, 2005). In the following calculations, we use our calculated density differences between the TTG gneiss and the subordinate lithologies at peak conditions (shaded areas, Fig. 4a–c) for $\Delta\rho$. This parameter is varied between model iterations to account for droplets comprised of the three different subordinate lithologies (BG, MG and UG) described above.

If the subordinate lithologies were emplaced by sagduction, the maximum depth reached by the droplet is constrained from estimates of pressure at peak P–T conditions. Based on our peak pressure estimate of 9 kbar, and using a density of the TTG gneiss at peak conditions (2.73 g cm^{-3}), this depth is taken as 33 km. Note that we are here assuming that the sagduction occurred from initial depths corresponding to the Earth's surface. However, there is a linear trade-off between depth attained and event duration. Therefore, sagduction from other levels within the upper crust is equivalent to the situation modelled, but with the time scaled by the same factor as the proportion of the total depth at which the body originated. For example, if sagduction initiated at a depth half way between the surface and the emplacement level, then the model result would be the equivalent of those displayed below, but with the timescale increased by a factor of two (because the droplet would be falling at half the modelled rate). We show below that changes in the value of the event timescale of this nature have a negligible effect on the model results, with two orders of magnitude of timescale having a limited effect on the results compared to the other parameters.

Depth is used in conjunction with an event duration, which is varied in successive calculations, to provide an average velocity, taken to be equal to the droplet's sinking velocity (v) for each duration considered. Thus, the fluid viscosity required for the droplet to sagduct can be calculated from Eq. 1. Event duration (controlling droplet velocity), droplet radius, and droplet lithology are all varied in the following calculations, so we are able to estimate the viscosity required for sagduction for each combination of parameters. Strain rate in the fluid ($\dot{\epsilon}$) is calculated from droplet velocity and radius as $\dot{\epsilon} = v/r$ because the strain due to the sinking droplet is accommodated in a deformed zone of the fluid of the same length-scale as the droplet radius (Batchelor, 1967).

Using mineral flow-laws (Rutter and Brodie, 2004; Rybacki et al., 2006), we can then investigate what temperature, fluid (i.e. TTG gneiss) mineralogy, and water content would result in the fluid having the viscosity calculated above, and thus what conditions would allow sagduction to occur for each combination of parameter values. These experimentally-derived mineral flow laws have the form

$$\eta = \dot{\epsilon}^{\frac{1}{n}-1}\left[\frac{1}{Ad^{-m}f_{H_2O}^{w}e^{-\frac{(Q+PV)}{RT}}}\right]^{\frac{1}{n}} \quad (2)$$

where A is a material constant, d is the grain size, m is the grain size exponent, f_{H_2O} is the water fugacity, w is the fugacity exponent, Q is the activation energy, P is the pressure, V is the activation volume, R is the molar gas constant, T is the temperature, and n is the stress exponent. A dislocation creep regime is assumed, given the large grain sizes present in Lewisian peak assemblages (e.g. Johnson et al., 2012; Rollinson, 2012) and the undulose extinction observed in samples considered in this study (Section 3), which means that m is zero and grain size is unimportant. Based upon the dominant mineralogy of the TTG gneiss (Fig. 5b), we use flow laws for wet and dry anorthite (Rybacki et al., 2006), and wet quartz (Rutter and Brodie, 2004). Whilst a specific flow law for dry quartz could not be found, it can be approximated by using low water contents in the flow law for wet quartz. Due to this uncertainty, 'dry' quartz is omitted from the figures in the following section for clarity, but it should be noted that it generally plots between the flows laws for wet quartz and dry anorthite. We have used the pure anortite flow-laws, due to them being the most well-constrained of the plagioclase compositions. However, we note that, where known, other plagioclase compositions have similar experimentally-derived rheologies (Rybacki and Dresen, 2004).

Water fugacity is unimportant when considering dry cases, as w is 0 for all dry flow laws. Water fugacity at water saturated conditions is taken to be 1.4 GPa, calculated at 950 °C, 9 kbar using the Pitzer and Sterner, 1994 equations of state through the Wither's fugacity calculator (https://www.esci.umn.edu/people/researchers/withe012/fugacity.htm). This is a maximum value for water fugacity, which decreases with deceasing pressure and temperature. Output viscosity is largely unaffected by our choice of pressure, as activation volumes are too low for the pressure term to be important at crustal depths. As such, peak pressure is used in the flow laws.

To explore the parameter space in which sagduction may occur, we vary four main parameters between model iterations. The radius of the droplet is varied in the range 0.1–100 km, although we note that in the LGC the subordinate lithologies are generally 0.01–5 km in size. The duration of the sagduction event has been varied in the range 10–500 Myr, to encompass the range of proposed timescales of high-grade LGC metamorphism (e.g. Whitehouse and Kemp, 2010; Taylor et al., 2020; Fischer et al., 2021). Three different possible lithologies (and so density contrasts) are considered for the droplet; BG, MG and UG. Finally, the wet and dry anorthite and quartz flow laws are used for the TTG gneiss. We first describe one iteration of the model and then extend the model across the parameter space.

6.2. Model results

One iteration of the model is illustrated in Fig. 7. A BG droplet lithology is used, which sets the density difference between the solid droplet and the fluid. A droplet radius (1000 m) and an event duration (50 Myr) are also imposed, resulting in a calculated strain rate of 2×10^{-14} s^{-1} (within the range that is commonly geologically inferred; Fagereng and Biggs, 2019). The fluid (TTG gneiss) viscosity that is calculated to allow the imposed rate of motion under these conditions, using Eq. 1, is shown by a black vertical line ($1.1x10^{19}$ Pa s). We have used the calculated strain rate to quantify how the viscosity predicted by the mineral flow laws varies with temperature using Eq. 2 (shown as curved lines). The intercept between required fluid viscosity and mineral flow law curves represents the temperature required to allow the sagduction event to take place, given the choices of lithology, radius, and duration. In this case, temperatures would need to be > 1000 °C for all mineral flow laws relevant to the TTG gneiss. We have here assumed a constant temperature, and so viscosity, during the sagduction event. We describe below how these results relate to the constraints on, and effects of, the variation of temperature with depth in the LGC.

We have carried out the above process for the three considered droplet compositions and a wide range of droplet radii and event durations, and here combine these results. Fig. 8 summarises model output in the same format as Fig. 7 for the full range of parameters. Results are shown for the three droplet lithologies considered at snapshots of

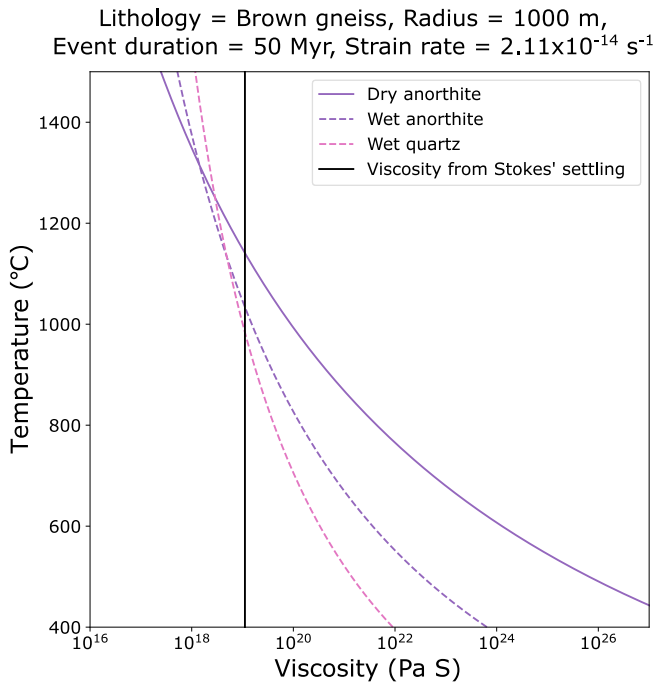

Fig. 7. Example output for one iteration of the sagduction model for a BG droplet of 1000 m radius that takes 50 Myr to move from the surface to peak depth.

varying droplet size versus and event duration. Calculated fluid strain rate ($\dot{\epsilon}$) and required fluid viscosity (η) are noted for each scenario.

Fig. 9a–c summarises the conditions under which sagduction can occur for each droplet lithology, by plotting the intercepts of required viscosity with mineral flow law curves for all iterations of the model (i.e. where the vertical black lines intercept each flow-law curve in Fig. 8). The width of the bands represent different event durations, with the upper bound representing 10 Myr and the lower bound 500 Myr. Longer event durations result in slightly cooler conditions being permitted. This effect is due to event duration controlling the strain rate. Longer events lead to lower strain rates, and therefore higher viscosities (and so cooler conditions) being compatible with a given size and density of sinking droplet. However, this effect is partially counteracted by a reduced strain rate resulting in an increased viscosity for a given temperature for mineral flow laws of the form in Eq. 2. The density difference between fluid and solid droplet has a larger effect. Increasing density difference reduces the temperature at which sagduction can occur, as the force acting on the droplet is increased, thus increasing the fluid viscosity required for a given strain rate, and therefore reducing the temperature required. This effect is explored in Fig. 9d, where, for the dry anorthite and wet quartz flow laws, and an event duration of 100 Myr, the results for BG, MG and UG lithologies are compared. This figure shows that temperatures 100–200 °C hotter are required for BG compared to UG and MG, because of the lower density contrast with the TTG gneiss. Droplet radius also exerts a strong control on the temperature required for sagduction, as larger bodies experience a greater force. Water content also has a strong control on the temperatures at which sagduction is an important process, with differences between wet and dry scenarios in the anorthite case on the order of 200–300 °C.

The largest observed outcrops of subordinate lithologies in the LGC have radii $< \sim 2$ km, shown by a dashed vertical line in Fig. 9a–c. Therefore, for sagduction to responsible for the emplacement of these bodies, temperatures are required to be 600–750 °C for UG to BG falling through wet quartz, 750–850 °C for wet anorthite, and 900–1000 °C for dry anorthite. Smaller bodies require higher temperatures. For example, a droplet one order of magnitude smaller than the largest droplet (i.e. with radius 200 m, shown by a vertical dotted line), gives an increase in the temperature required for sagduction to occur of 200–300 °C. Below, we discuss conditions in the LGC, and therefore whether sagduction was an important process in this region.

7. Discussion

The work presented above allows interrogation of the effects of a range of different parameters on whether sagduction is an important process (i.e. whether it could have been responsible for emplacing the subordinate lithologies within the Lewisian central region TG). The results presented in Fig. 9, although calculated for LGC lithologies, are generally applicable to other Archean terranes owing to the lithologies considered in this paper being common in grey gneiss terranes. Here we first consider sagduction importance within the LGC, and consider in turn the main model parameters (size, temperature, mineralogy, water content), and then the utility of the model in constraining sagduction importance more generally.

7.1. Constraining the importance of sagduction in the Lewisian Gneiss Complex

Some constraints on the appropriate model parameters for the LGC can be made from field observations. Throughout this discussion, where uncertainties are present, we select parameter values that favour the effectiveness of sagduction, to establish if any situations result in this process being important. Droplet radii are constrained on the basis of mapped occurrences of subordinate lithologies in the LGC central region (Fig. 1b). Cnoc an t-Sidhean is the largest subordinate lithology outcrop within the central region and has a radius of ~2 km (dashed line on Fig. 9). No lower bound is placed on droplet radius as subordinate lithologies are observed within the Lewisian on all $<$ 2 km scales (e.g. Peach et al., 1907).

If these bodies were emplaced by sagduction, their radius observed today within the Lewisian may not accurately represent the initial sizes of droplets dripping from a high density upper layer. Modifications could occur due to deformation during sagduction, such that when looking at the mid–lower crust, we may be observing small fragments of initially larger sagducted bodies (Johnson et al., 2016). However, most outcrops of subordinate lithologies within the TTG gneiss do not show evidence of mixing or disaggregation into the TTG gneiss (e.g. Cartwright et al., 1985; Guice et al., 2020), making a fragmented droplet origin for these bodies unlikely. Later tectonic events may also modify observed droplet size, for example the Cnoc an t-Sidhean locality lies between two shear zones and shows evidence of having been elongated along the strike of the Stoer shear zone (Fig. 1c). Other subordinate lithology bodies also lie in or near noted shear zones (e.g. the Laxford shear zone in Fig. 1b). As such, field mapping could incorrectly estimate droplet radius. To account for this effect the longest axis of the elongate Cnoc an t-Sidhean locality is considered, possibly resulting in an overestimate of droplet radius (which would favour sagduction effectiveness).

In the modelling above we assumed a constant viscosity, and so constant temperature, in the TTG gneiss. The shape of the Archean LGC geotherm, and its evolution through time, are not known, but the available information is: (1) a constraint on maximum temperature for the current erosion level of 950 °C is imposed from the peak *P–T* conditions discussed above; (2) loose estimates of the minimum possible average temperature in the crust overlying the present erosion level can be made if we assume a linear geotherm and the peak *T* from (1), resulting in an average temperature of 475 °C in the overlying material; (3) alternatively, if the geotherm is curved, with higher thermal gradients near the surface, the vertically-averaged temperature will be higher, with an upper bound approaching the peak *T* for the case of a very steep surface geothermal gradient above an isothermal mid-crust; (4) the higher structural levels preserved in the northern and southern blocks of the LGC, and accompanying amphibolite-facies assemblages

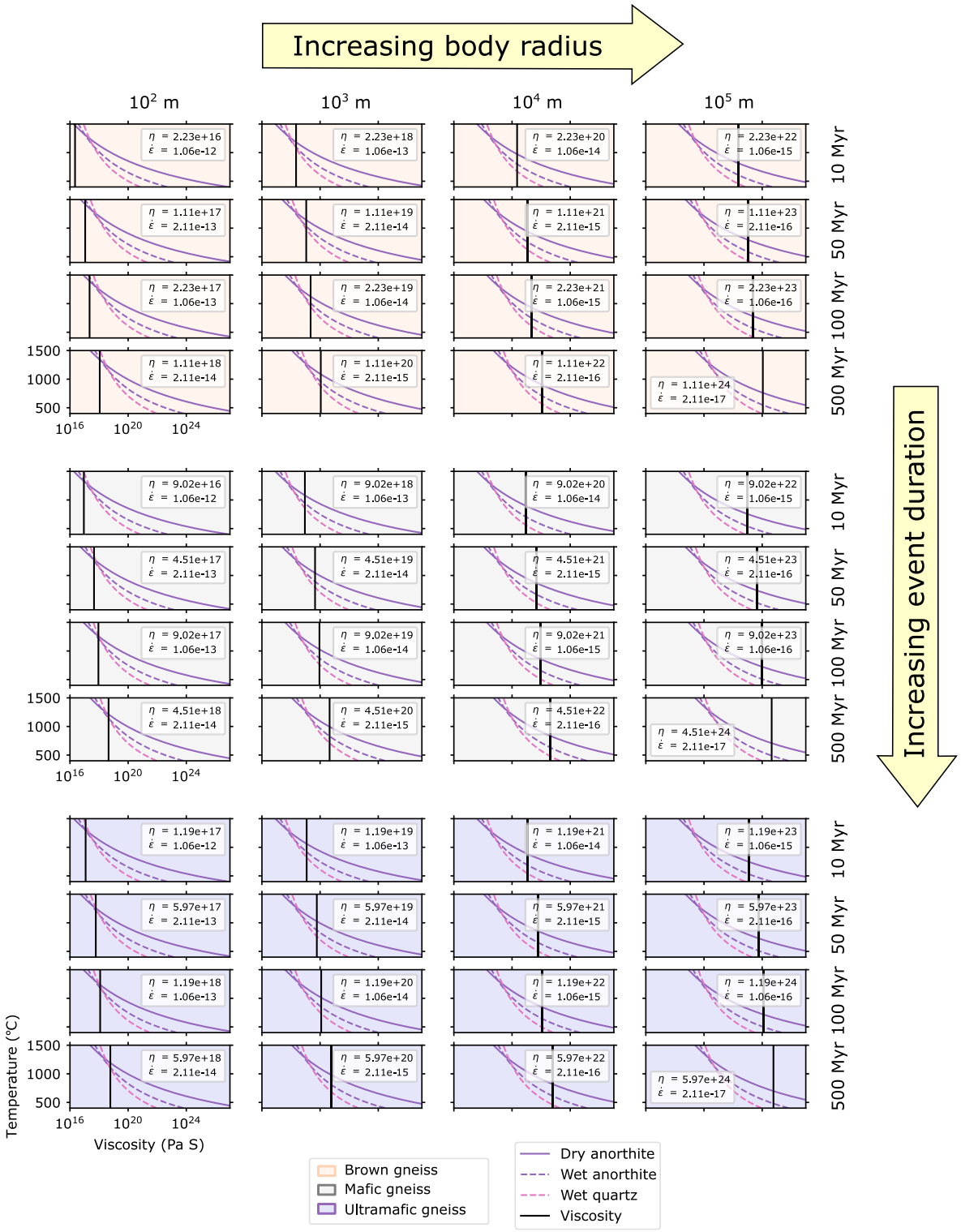

Fig. 8. Sagduction model output across explored parameter space. Salmon boxes show results for a droplet of BG (i.e. minimum droplet-fluid density difference), grey boxes show results for a MG droplet and purple boxes show results for a UG droplet (maximum droplet-fluid density difference). Plots are shown for a range of droplet sizes (increases left to right) and event durations (increases downwards). The black line on each plot is the viscosity calculated from Stokes' settling law for a droplet with the parameters for that scenario. This viscosity (Pa S) and the fluid strain rate (s^{-1}) are labelled for each scenario. The curves are mineral flow laws showing how viscosity varies with temperature for the strain rate calculated for each scenario. The intercept of the black line with each flow law curve gives the temperature that would be required for sagduction to occur, with this temperature varying significantly depending on the composition of the droplet and the flow laws used to model the TTG gneiss.

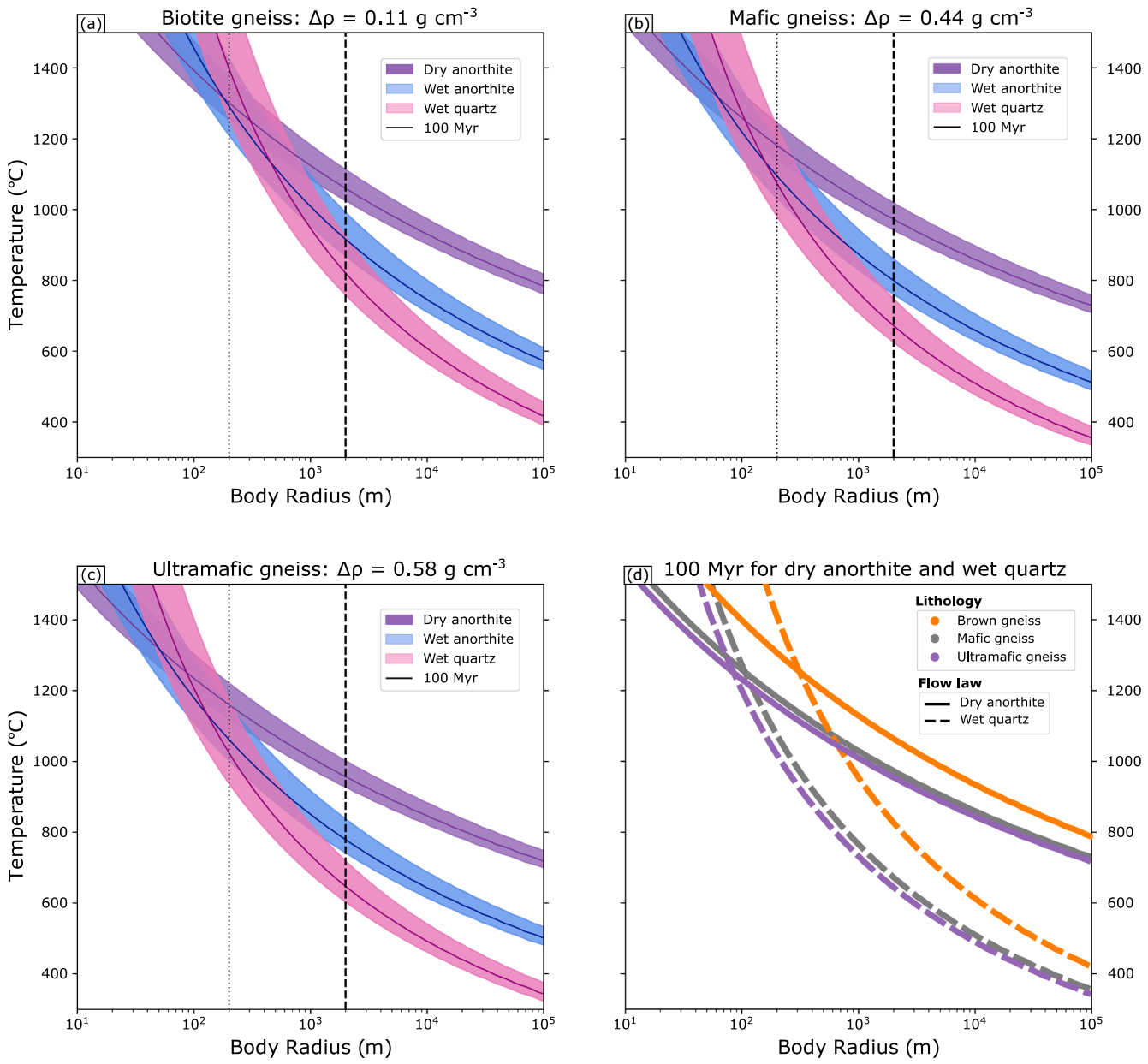

Fig. 9. (a–c) Curves show what temperature would be needed for a droplet of given radius to reach the model maximum depth. Each band is contoured for event duration, with the top margin of a band representing a 10 Myr scenario, the central line a 100 Myr scenario and the bottom margin a 500 Myr scenario. The vertical black dashed line shows an upper bound on droplet radius in the LGC at 2 km, and the black dotted line shows a droplet with 200 m radius. **(d)** Compilation of 100 Myr event durations for dry anorthite and wet quartz flow laws illustrating how density differences affect temperatures required for sagduction (see text for details).

(Peach et al., 1907; Sutton and Watson, 1951; Park and Tarney, 1987), imply a case intermediate between (2) and (3). Below we compare these LGC temperature estimates with those that would be required for sagduction to be important.

Having considered droplet size and the prevailing temperatures, we now consider the TTG gneiss mineralogy. The major phase mineralogy of TTG gneiss lithologies does not markedly change across the considered *P–T* conditions (Fig. S2, Table S7), as is typical for meta-granitoids (e.g. Palin et al., 2017). Fig. 5a,b shows that TTG gneiss are generally dominated by feldspar, on average containing 62 vol.%, with plagioclase contents from 30–67 vol.% (average 55 vol.%) and K-feldspar from 0–33 vol.% (average 6.6 vol.%). Quartz is the second most abundant mineral at 6–38 vol.% (average 24 vol.%). The viscosity of the TTG gneiss will therefore lie somewhere between quartz and feldspar rheologies, with feldspar generally making up a high enough volume of the TTG gneiss such that it is expected to form an interconnected network that dominates sample viscosity (Shinevar et al., 2015). Prior to peak metamorphic conditions, partial melting of the TTG gneiss will have occurred, and volatiles (including water) would be expected to be concentrated into the melt. If the subordinate lithologies were emplaced after the onset of TTG gneiss melting, we would therefore expect the TTG gneiss to be characterised by a 'dry' anorthite rheology (purple bands on Fig. 9). This logic is consistent with the observations of Menegon et al., 2011, who found that at similar *P–T* conditions, any remaining water was structurally bound in hydrous phases present in low proportions, and the nominally anyhdrous minerals were truly anhydrous to the tens of ppm level. Alternatively, if the subordinate lithologies were emplaced before partial melting, then the relevant rheology would be that of 'wet' anorthite, and the relevant temperatures would need to be lower than the solidus (i.e. <600–700 °C; Watkins et al., 2007). For the case of 'wet' flow laws, the temperature required for sagduction depends on the water fugacity used, as shown in Fig. S4.

In the calculation above, a water fugacity thought to represent water saturated conditions (1.4 GPa) was used, to consider the most favourable conditions for sagduction. Figure S4 illustrates that reducing water fugacity from saturated to near-anhydrous results in an increase in temperature required for sagduction to occur.

It is also necessary to consider, for the case of partial melting of the TTG gneiss, whether the melt itself could lower the viscosity and enable sagduction to occur more effectively. Melt volume, both at peak conditions and during sagduction, is poorly constrained. Whilst it is generally accepted that the Lewisian underwent melting (e.g. Zirkler et al., 2012; Johnson et al., 2012; Johnson et al., 2013), it is uncertain how much melt remained in the mid–lower crust, and for how long melt generation occurred. The presence of small melt volumes within the TTG gneiss could act to reduce the viscosity of the bulk TTG gneiss at a given temperature, which would reduce the temperature required for sagduction. However, it is unlikely that significant volumes of melt persisted over a sufficiently large depth range at any given time to appreciably affect the importance of sagduction, for example because of the scarce evidence of in situ crystallised melt (Johnson et al., 2013). The preservation of granulite-facies rocks, as observed in the central region, also requires effective melt extraction and transport away from the source regions (White and Powell, 2002).

Based on the above discussion, we here examine whether sagduction is feasible for the LGC. For the case of an anhydrous anorthite rheology, temperatures in excess of 950 °C (for the high density UG) to 1050 °C (for the lower density BG) are required for a droplet of radius 2 km, with temperatures required increasing to in excess of 1100–1250 °C for a 200 m droplet. Such temperatures just overlap the peak conditions for the largest LGC body in the UG case. However this scenario is not considered viable, as the largest UG body has a radius of < 1 km, requiring a higher temperature of 1000 °C. Additionally, as discussed above, it is unlikely that the crust is entirely at the peak temperature. For all other scenarios of droplet composition and size, the required temperatures are above peak conditions, so significantly above the temperatures that are likely to have been experienced during sagduction. These results show that sagduction is not important in the LGC if the TTG gneiss is characterised by an anhydrous anorthite rheology.

For sub-solidus conditions and a hydrous anorthite rheology, the equivalent temperatures are 750 °C (for the UG) to 850 °C (for the BG) for a 2 km droplet, and 1000–1200 °C for a 200 m droplet. These temperatures are above the wet solidus (600–700 °C; Watkins et al., 2007) and therefore incompatible with the use of a wet flow law. Additionally, as above, sustaining these temperatures throughout the crust over the event duration is incompatible with available constraints from the LGC. If the TTG gneiss were more quartz-rich than observed in the LGC, and were hydrous, required temperatures are reduced to 600–750 °C for a 2 km droplet and 900–1200 °C for a 200 m droplet (mostly above the wet solidus). As described above, the values for dry quartz will be similar to those for wet feldspar. Even in this hypothetical situation of a quartz-dominated LGC, in all but the extreme cases of the largest and densest possible bodies, available temperature constraints are incompatible with those required. Additionally even in this case, sagduction could not explain the numerous small bodies of subordinate lithologies on sub 100 m scales throughout the LGC (e.g. Fig. 1c,d; Davies, 1976; Guice et al., 2020).

Collectively, this logic implies that the presence of the observed subordinate lithologies within the LGC are not the result of sagduction, despite our model setup and choices of poorly constrained parameters that favour the effectiveness of this process. We therefore suggest that the subordinate lithologies are instead the result of uniformitarian processes, such as igneous emplacement at depth (Bowes et al., 1964; Guice et al., 2018a; Guice et al., 2020), and/or transport from higher crustal levels by faulting. Further work is required to determine the level of formation of the subordinate lithologies in the LGC, thus vertical transport distances required (Cartwright et al., 1985; Zirkler et al., 2012; Johnson et al., 2016), but regardless of the scenario, sagduction is not viable to explain the structural evolution of the LGC. This discussion has similarities with the controversies regarding ophiolite emplacement at the present-day. Although the detailed mechanisms are unclear, presently active tectonic processes are able to emplace dense ultramafic bodies into the continental crust (Moores, 1982).

7.2. Validity of model in other Archean terranes

In addition to applying our approach to mid–lower crustal grey gneiss terranes, as demonstrated above for the LGC, our model could also be used in Archean granite-greenstone belts where sagduction has been suggested as a means of emplacing the greenstones within the granite. An outcrop style observed in some areas of granite-greenstone belts is a dome-and-basin pattern, whereby greenstone belts form variably shaped bands between gneiss/granite domes (Anhaeusser, 2014). Such regions include: the Pilbara Craton in Australia (Hickman and van Kranendonk, 2012; François et al., 2014; van Kranendonk et al., 2015; Wiemer et al., 2018); the Kaapvaal Craton in South Africa (van Kranendonk et al., 2014; Johnson et al., 2014; van Kranendonk, 2021); the Superior Province in Canada (Bedard et al., 2003; Lin et al., 2013); the North China Craton (Liu and Wei, 2020); and the Dharwar craton in India (Bouhallier et al., 1993).

To assess the importance of sagduction in this scenario, we therefore need to know the compositions and sizes of the greenstone bodies, and the composition of the granite. The greenstone components of granite-greenstone belts are lithologically diverse; comprised of sedimentary, volcanic and plutonic rocks with a wide range of compositions and potential histories (e.g. Anhaeusser, 2014). Their density is therefore likely to be in the range between the BG to MG (the lithologies discussed above in relation to the LGC), depending on the relative proportion of metasedimentary and metavolcanic rocks. The granite and gneissic components adjacent to greenstones range compositionally from TTG to granite (Moyen, 2011; Anhaeusser, 2014), and will have similar densities to the TTG gneiss discussed above for the LGC. The largest reported possible sagducted 'droplets' (e.g. van Kranendonk et al., 2015) occur in the Pilbara belt and have widths of 50 km, which we approximate as a radius of a sinking drop of 25 km. However, it should be noted that the original stratigraphic thicknesses and structure of greenstone belts, such as Pilbara, are extensively debated (with many authors preferring extensive folding or thrust faulting of < 10 km original sequences; e.g. de Wit, 1982; Kusky et al., 2021 and references therein).

Using the values above and Fig. 9a–c, a–c, for the case of an anhydrous anorthite rheology of the gneiss/granite and our maximum considered duration of 500 Myr, temperatures required are in excess of 775 °C (for the high density MG) to 850 °C (for the lower density BG). For a hydrous feldspar rheology, the equivalent temperatures are 550 °C (for the MG) to 650 °C (for the BG). For a quartz dominated gneiss/granite, a hydrous quartz rheology give temperatures temperatures of 425 °C (for the MG) to 500 °C (for the BG).

Greenstone belts vary from near-unmetamorphosed, to having experienced polyphase deformation and metamorphism. Many large greenstone belts now exposed at the surface were metamophosed at greenshist- to lower amphibolite-facies (300–550 °C; e.g. Brandl et al., 2006; François et al., 2014; Mühlberg et al., 2021), although there are occasional examples up to granulite-facies (e.g. Garde et al., 2020). These higher grade events are often interpreted as occurring after granite-greenstone belt formation (Anhaeusser, 2014), potentially also leading to thickening of the belts. The temperatures required for sagduction to be important are therefore largely in excess of those observed, suggesting sagduction is not viable at conditions typical of granite-greenstone belts. Additionally, these temperatures are increased by ~100–200 °C if body radius is reduced to ~5 km, based upon prior suggestions of the mapped greenstone widths being the result of post-emplacement thickening. The required temperatures are also increased by 100 °C if an event timescale of 10 Myr is used instead of considering the maximum bound of 500 Myr.

Overall these considerations suggest sagduction is unlikely to be important in most greenstone-granite belts. However, we note that specific evidence from individual terranes, such as the timescale of melting and the degree of melt connectivity throughout the crust, should be taken into account when considering in detail sagduction viability in a given region (as we considered for the Lewisian in Section 7.1). Our conclusion regarding the difficulty of forming granite-greenstone terranes by sagduction is consistent with uniformitarian Archean tectonics, and is in line with a number of recent studies proposing uniformitarian explanations for dome-and-basin structures in Archean granite-greenstone belts. Possible mechanisms that have been suggested include fold interference during terrane accretion and mountain-building (Kusky et al., 2021) and fault bounded core-complexes; e.g. Pilbara, Australia (e.g. van Haaften and White, 1998); Nhlangano gneiss dome, Eswatini (Hofmann et al., 2015). Uniformitarian Archean tectonics are also consistent with observations from granite-greenstone belts that do not show evidence of dome-and-basin structures, such as in the Greenland portion of the North Atlantic Craton, and are proposed to have an oceanic or volcanic arc origin (Polat et al., 2015, Garde et al., 2020; Nutman et al., 2021, and references therein). Kusky et al., 2021 also reviewed granite-greenstone belts without dome-and-keel morphology (Isua, Greenland; Nulliak Belt, Canada; Nuvvuagittuq, Canada) and concluded that these regions are also consistent with an accretionary arc origin.

Although beyond the scope of this study, our approach to constraining the conditions required for density driven segregation is also applicable to the present day. Such segregation is thought to be a means of fractionation and crustal growth in volcanic arcs (e.g. Hacker et al., 2011; Behn et al., 2011), allowing the formation of intermediate-composition crust from mafic mantle melts. This scenario is physically equivalent to that discussed above, although extensions to the approach would be required. Olivine and pyroxene flow laws would need to be used, as these are applicable to the upper mantle or lower crustal mafic surroundings in which the segregation is thought to occur. Additionally, it would be necessary to model the evolving density of magma in this melt-dominated system.

8. Conclusions

We have combined petrology and mechanical modelling to assess the importance of sagduction in the Lewisian Gneiss Complex, and demonstrate how the approach can be used globally. We find that at plausible conditions of temperature and composition, sagduction is not viable as a means of emplacing the subordinate lithologies within the Lewisian TTG gneiss; instead we propose uniformitarian tectonic processes were at work. Additionally, the extension of our models to consider granite-greenstone belts implies that sagduction is unlikely to be important in the formation of those Precambrian structures.

Declaration of Competing Interest

The authors declare that they have no known competing financial interests or personal relationships that could have appeared to influence the work reported in this paper.

Acknowledgements

SRM is funded by a 'C-CLEAR' NERC DTP studentship (NE/S007164/1). SRM thanks Christ's College, Cambridge for providing funding for fieldwork. This work was partly supported by COMET, which is the NERC Centre for the Observation and Modelling of Earthquakes, Volcanoes and Tectonics, a partnership between UK Universities and the British Geological Survey.

Appendix A. Supplementary data

Supplementary data to this article can be found online at https://doi.org/10.1016/j.precamres.2022.106708.

References

Anhaeusser, C.R., 2014. Archaean greenstone belts and associated granitic rocks – A review. J. Afr. Earth Sc. 100, 684–732. https://doi.org/10.1016/j.jafrearsci.2014.07.019.

Attfield, P. (1987), The structural history of the Canisp Shear Zone, in Evolution of the Lewisian and Comparable Precambrian High Grade Terrains, edited by R. Park & J. Tarney, pp. 165–173, Geological Society Special Publication, doi: 10.1144/GSL.SP.1987.027.01.14.

Batchelor, G., 1967. An Introduction to Fluid Dynamics, 230–234 pp.,. Cambridge University Press.

Beach, A., 1973. The mineralogy of high temperature shear zones at Scourie, N.W. Scotland, Journal of Petrology 14, 231–248. https://doi.org/10.1093/petrology/14.2.231.

Bedard, J.H., 2006. A catalytic delamination-driven model for coupled genesis of Archaean crust and sub-continental lithospheric mantle. Geochim. Cosmochim. Acta 70, 1188–1214. https://doi.org/10.1016/j.gca.2005.11.008.

Bedard, J.H., 2018. Stagnant lids and mantle overturns: Implications for Archaean tectonics magmagenesis, crustal growth, mantle evolution, and the start of plate tectonics. Geosci. Front. 9, 19–49. https://doi.org/10.1016/j.gsf.2017.01.005.

Bedard, J.H., Brouillette, P., Madore, L., Berclaz, A., 2003. Archaean cratonization and deformation in the northern Superior Province, Canada: an evaluation of plate tectonic vs vertical tectonic models. Precambr. Res. 127, 61–67. https://doi.org/10.1016/S0301-9268(03)00181-5.

Behn, M., Kelemen, P., Hirth, G., Bradley, R., Massonne, H., 2011. Diapirs as the source of the sediment signature in arc lavas. Nat. Geosci. 4, 641–646. https://doi.org/10.1038/ngeo1214.

Bouhallier, H., Choukroune, P., Ballèvre, M., 1993. Diapirism, bulk homogeneous shortening and transcurrent shearing in the Archaean Dharwar craton: the Holenarsipur area, southern India. Precambr. Res. 63, 43–58. https://doi.org/10.1016/0301-9268(93)90004-L.

Bowes, D., Wright, A., Park, R., 1964. Layered intrusive rocks in the Lewisian of the North-West Highlands of Scotland. Quart. J. Geoc 120, 153–192. https://doi.org/10.1144/gsjgs.120.1.0153.

Boyd, F., Mertzman, S., 1987. Composition and structure of the Kaapvaal lithosphere, Southern Africa, Magmatic processes; physicochemical principles. Geochemical Society 1, 13–24.

Brandl, G., Cloete, M., & Anhaeusser, C. (2006), Archaean greenstone belts, in The Geology of South Africa, edited by M.R. Johnson, C.R. Anhaeusser, & R.J. Thomas, pp. 9–56, Geological Society of South Africa, Johannesburg and Council for Geoscience.

Burgmann, R., Dresen, G., 2008. Rheology of the Lower Crust and Upper Mantle: Evidence from Rock Mechanics, Geodesy, and Field Observations, Annual Reviews of Earth and Planetary. Science 36, 531–567. https://doi.org/10.1146/annurev.earth.36.031207.124326.

Cartwright, I., Fitches, W., O'Hara, M., Barnicoat, A., O'Hara, S., 1985. Archaean supracrustal rocks from the Lewisian near Stoer. Sutherland, Scottish Journal of Geology 21, 187–196. https://doi.org/10.1144/sjg21020187.

Cawood, P.A., Hawkesworth, C.J., Pisarevsky, S.A., Dhuime, B., Capitanio, F.A., Nebel, O., 2018. Geological archive of the onset of plate tectonics. Philosophical Transactions of the Royal Society A 376 (20170), 405. https://doi.org/10.1098/rsta.2017.0405.

Collins, W., Kranendonk, M.V., Teyssier, C., 1998. Partial convective overturn of Archaean crust in the east Pilbara Craton, Western Australia: driving mechanisms and tectonic implications. J. Struct. Geol. 20, 1405–1424. https://doi.org/10.1016/S0191-8141(98)00073-X.

Davies, F., 1976. Early Scourian structures in the Scourie-Laxford region and their bearing on the evolution of the Laxford Front. J. Geol. Soc. 132, 543–554. https://doi.org/10.1144/gsjgs.132.5.0543.

Davies, J., Heaman, L., 2014. New U-Pb baddeleyite and zircon ages for the Scourie dyke swarm: a long-lived large igneous province with implications for the Paleoproterozoic evolution of NW Scotland. Precambr. Res. 249, 180–198. https://doi.org/10.1016/j.precamres.2014.05.007.

de Capitani, C., Petrakakis, K., 2010. The computation of equilibrium assemblage diagrams with Theriak/Domino software. Am. Mineral. 95, 1006–1016. https://doi.org/10.2138/am.2010.3354.

de Villeneuve, V., Aarts, D., Lekkerkerker, H., 2006. Comparing the approach of a rigid sphere and a deformable droplet towards a deformable fluid surface. Colloids Surf., A 282–283, 61–67. https://doi.org/10.1016/j.colsurfa.2006.01.035.

de Wit, M., 1982. Gliding and overthrust nappe tectonics in the Barberton greenstone belt. J. Struct. Geol. 4, 117–136 doi:https://doi.org/10.25131/sajg.124.0017.

Dimanov, A., Dresen, G., 2005. Rheology of synthetic anorthite-diopside aggregates: implications for ductile shear zones, Journal of Geophysical Research, 110. B 07, 203. https://doi.org/10.1029/2004JB003431.

Eggers, J., Villermaux, E., 2008. Physics of liquid jets. Rep. Prog. Phys. 71 (036), 601. https://doi.org/10.1088/0034-4885/71/3/036601.

Elgowainy, A., Ashgriz, N., 1997. The Rayleigh-Taylor instability of viscous fluid layers. Phys. Fluids 9, 1635. https://doi.org/10.1063/1.869283.

Fagereng, Å., Biggs, J., 2019. New perspectives on 'geological strain rates' calculated from both naturally deformed and actively deforming rocks. J. Struct. Geol. 125, 100–110. https://doi.org/10.1016/j.jsg.2018.10.004.
Feisel, Y., White, R., Palin, R., Johnson, T., 2018. New constraints on granulite facies metamorphism and melt production in the Lewisian Complex, northwest Scotland. J. Metamorph. Geol. 36, 799–819. https://doi.org/10.1111/jmg.12311.
Fischer, S., Prave, A., Johnson, T.E., Cawood, P., Hawkesworth, C.J., Horstwood, M., EIMF, 2021. Using zircon in mafic migmatites to disentangle complex high-grade gneiss terrains – Terrane spotting in the Lewisian complex. NW Scotland, Precambrian Research 355 (106), 074. https://doi.org/10.1016/j.precamres.2020.106074.
François, C., Philippot, P., Rey, P., Rubatto, D., 2014. Burial and exhumation during Archean sagduction in the East Pilbara Granite-Greenstone Terrane. Earth Planet. Sci. Lett. 396, 235–251. https://doi.org/10.1016/j.epsl.2014.04.025.
Friend, C.R.L., Kinny, P.D., 1995. New evidence for protolith ages of Lewisian granulites, northwest Scotland. Geology 23, 1027–1030. https://doi.org/10.1130/0091-7613(1995)023<1027:NEFPAO>2.3.CO;2.
Furnes, H., T, D., & de Wit, M. (2015), Precambrian greenstone sequences represent different ophiolite types, Gondwana Research, 27, 649–685, doi:https://doi.org/10.1016/j.gr.2013.06.004.
Garde, A., Windley, B., Kokfelt, T., Keulen, N., 2020. Tectonics in the North Atlantic Craton of West Greenland Revealed by Well Exposed Horizontal Crustal Tectonics, Island Arcs and Tonalite-Trondhjemite-Granodiorite Complexes. Frontiers of Earth Science 8 (540), 997. https://doi.org/10.3389/feart.2020.540997.
Goodenough, K., Crowley, Q., Krabbendam, M., Parry, S., 2013. New U-Pb age constraints for the Laxford shear zone. NW Scotland: Evidence for tectono-magmatic processes associated with the formation of a Paleoproterozoic supercontinent, Precambrian Research 233, 1–19. https://doi.org/10.1016/j.precamres.2013.04.010.
Green, E., White, R., Diener, J., Powell, R., Holland, T., Palin, R., 2016. Activity-composition relations for the calculation of partial melting equilibria in metabasic rocks. J. Metamorph. Geol. 34, 845–869. https://doi.org/10.1111/jmg.12211.
Guice, G., McDonald, I., Hughes, H., MacDonald, J., Blenkinsop, T., Goodenough, K., Faithfull, J., Gooday, R., 2018a. Re-evaluating ambiguous age relationships in Archean cratons: Implications for the origin of ultramafic-mafic complexes in the Lewisian Gneiss Complex. Precambr. Res. 311, 136–156. https://doi.org/10.1016/j.precamres.2018.04.020.
Guice, G., McDonald, I., Hughes, H., Schlatter, D., Goodenough, K., MacDonald, J., Faithfull, J., 2018b. Assessing the Validity of Negative High Field Strength-Element Anomalies as a Proxy for Archaean Subduction: Evidence from the Ben Strome Complex, NW Scotland. Geosciences 8, 338. https://doi.org/10.3390/geosciences8090338.
Guice, G., McDonald, I., Hughes, H., MacDonald, J., Faithfull, J., 2020. Origin(s) and geodynamic significance of Archean ultramafic– mafic bodies in the mainland Lewisian Gneiss Complex, North Atlantic Craton. J. Geol. Soc. 177, 700–717. https://doi.org/10.1144/jgs2020-013.
Hacker, B.R., Kelemen, P., D.Behn, M., 2011. Differentiation of the continental crust by relamination. Earth Planet. Sci. Lett. 307, 501–516. https://doi.org/10.1016/j.epsl.2011.05.024.
Heaman, L., Tarney, J., 1989. U-Pb baddeleyite ages for the Scourie dyke swarm, Scotland – evidence for two distinct intrusion events. Nature 340, 705–708. https://doi.org/10.1038/340705a0.
Hickman, A., van Kranendonk, M., 2012. Early Earth evolution: evidence from the 3.5–1.8 Ga geological history of the Pilbara region of Western Australia. Episodes 35, 283–297 doi:https://doi.org/10.18814/epiiugs/2012/v35i1/028.
Hofmann, A., Kröner, A., Xie, H., Hegner, E., Belyanin, G., Kramers, J., Bolhar, R., Slabunov, A., Reinhardt, J., Horváth, P., 2015. The Nhlangano gneiss dome in south-west Swaziland – A record of crustal destabilization of the eastern Kaapvaal craton in the Neoarchaean. Precambr. Res. 258, 109–132. https://doi.org/10.1016/j.precamres.2014.12.008.
Holland, T., Powell, R., 2011. An improved and extended internally consistent thermodynamic dataset for phases of petrological interest, involving a new equation of state for solids. J. Metamorph. Geol. 29, 333–383. https://doi.org/10.1111/j.1525-1314.2010.00923.x.
Jennings, E., Holland, T., 2015. A Simple Thermodynamic Model for Melting of Peridotite in the System NCFMASOCr. J. Petrol. 56, 869–892. https://doi.org/10.1093/petrology/egv020.
Johnson, T., White, R., 2011. Phase equilibrium constraints on conditions of granulite-facies metamorphism at Scourie, NW Scotland. J. Geol. Soc. 168, 147–158. https://doi.org/10.1144/0016-76492010-069.
Johnson, T., Fischer, S., White, R., Brown, M., Rollinson, H., 2012. Archaean Intracrustal Differentiation from Partial Melting of Metagabbro—Field and Geochemical Evidence from the Central Region of the Lewisian Complex, NW Scotland. J. Petrol. 53, 2115–2138. https://doi.org/10.1093/petrology/egs046.
Johnson, T., Fischer, S., White, R., 2013. Field and petrographic evidence for partial melting of TTG gneisses from the central region of the mainland Lewisian complex, NW Scotland. J. Geol. Soc. 170, 319–326. https://doi.org/10.1144/jgs2012-096.
Johnson, T., Brown, M., Kaus, B., van Tongeren, J., 2014. Delamination and recycling of Archaean crust caused by gravitational instabilities. Nat. Geosci. 7, 47–52. https://doi.org/10.1038/ngeo2019.
Johnson, T., Brown, M., Goodenough, K., Clark, C., Kinny, P., White, R., 2016. Subduction or sagduction? Ambiguity in constraining the origin of ultramafic–mafic bodies in the Archean crust of NW Scotland. Precambr. Res. 238, 89–105. https://doi.org/10.1016/j.precamres.2016.07.013.
Johnson, T., Kirkland, C., Gardiner, N., Brown, M., Smithies, R., Santosh, M., 2019. Secular change in TTG compositions: Implications for the evolution of Archaean geodynamics. Earth Planet. Sci. Lett. 505, 65–72. https://doi.org/10.1016/j.epsl.2018.10.022.
Kim, S., & Karrila, S. (2005), Microhydrodynamics, 78–79 pp., Dover.
Kinny, P., 1997. U-Pb isotopic evidence for the accretion of different crustal blocks to form the Lewisian Complex of northwest Scotland. Contributions in Mineralogy and Petrology 129, 326–340. https://doi.org/10.1007/s004100050340.
Kinny, P., Friend, C., Love, G., 2005. Proposal for a terrane-based nomenclature for the Lewisian Gneiss Complex of NW Scotland. J. Geol. Soc. 162, 175–186. https://doi.org/10.1144/0016-764903-149.
Korenaga, J., 2013. Initiation and Evolution of Plate Tectonics on Earth: Theories and Observations. Annu. Rev. Earth Planet. Sci. 41, 117–151. https://doi.org/10.1146/annurev-earth-050212-124208.
Kusky, T., Windley, B., Polat, A., 2018. Geological evidence for the operation of plate tectonics throughout the Archean: Records from Archean paleo-plate boundaries. Journal of Earth Science 29, 1291–1303. https://doi.org/10.1007/s12583-018-0999-6.
Kusky, T., Windley, B., Polat, A., Wang, L., Ning, W., Zhong, Y., 2021. Archean dome-and-basin style structures form during growth and death of intraoceanic and continental margin arcs in accretionary orogens. Earth Sci. Rev. 220 (103), 725. https://doi.org/10.1016/j.earscirev.2021.103725.
Lin, S., Parks, J., Heaman, L., Simonetti, A., Corkery, M., 2013. Diapirism and sagduction as a mechanism for deposition of 'Timiskaming-type' sedimentary sequences, Superior Province: evidence from detrital zircon geochronology and implications for the Borden Lake conglomerate exposed middle to lower crust in the Kapuskasing Uplift. Precambr. Res. 238, 148–157. https://doi.org/10.1016/j.precamres.2013.09.012.
Liu, T., Wei, C., 2020. Metamorphic P-T paths and Zircon U-Pb ages of Archean ultra-high temperature paragneisses from the Qian'an gneiss dome. East Hebei terrane, North China Craton, Journal of Metamorphic Geology 38, 329–356. https://doi.org/10.1111/jmg.12524.
Love, G., Kinny, P., Friend, C., 2004. Timing of magmatism and metamorphism in the Gruinard Bay area of the Lewisian Gneiss Complex: comparisons with the Assynt Terrane and implications for terrane accretion. Contributions in Mineralogy and Petrology 146, 620–636. https://doi.org/10.1007/s00410-003-0519-1.
Love, G., Friend, C., Kinny, P., 2010. Palaeoproterozoic terrane assembly in the Lewisian Gneiss Complex on the Scottish mainland, south of Gruinard Bay: SHRIMP U-Pb zircon evidence. Precambr. Res. 183, 89–111. https://doi.org/10.1016/j.precamres.2010.07.014.
Macdonald, J., Goodenough, K., Wheeler, J., Crowley, Q., Harley, S., Mariani, E., Tatham, D., 2015. Temperature-time evolution of the Assynt Terrane of the Lewisian Gneiss Complex of Northwest Scotland from zircon U-Pb dating and Ti thermometry. Precambr. Res. 260, 55–75. https://doi.org/10.1016/j.precamres.2015.01.009.
Menegon, L., Nasipuri, P., Stünitz, H., Behrens, H., Ravna, E., 2011. Dry and strong quartz during deformation of the lower crust in the presence of melt, Journal of Geophysical Research, 116. B 10, 410. https://doi.org/10.1029/2011JB008371.
Mühlberg, M., Stevensa, G., Moyen, J., Kisters, A., Lana, C., 2021. Thermal evolution of the Stolzburg Block, Barberton granitoid-greenstone terrain, South Africa: Implications for Paleoarchean tectonic processes. Precambr. Res. 359 (106), 082. https://doi.org/10.1016/j.precamres.2020.106082.
Moore, W., Webb, A., 2013. Heat-pipe earth. Nature 501, 501–505. https://doi.org/10.1038/nature12473.
Moores, E., 1982. Origin and Emplacement of Ophiolites. Rev. Geophys. 20, 735–760. https://doi.org/10.1029/RG020i004p00735.
Moreau, R., Happel, J., Brenner, H., 1981. Low Reynolds number hydrodynamics: with special applications to particulate media. Springer, Netherlands, pp. 119–234.
Moyen, J., 2011. The composite Archaean grey gneisses: Petrological significance, and evidence for a non-unique tectonic setting for Archaean crustal growth. Lithos 123, 11–36. https://doi.org/10.1016/j.lithos.2010.09.015.
Moyen, J., Martin, H., 2012. Forty years of TTG research. Lithos 148, 312–336. https://doi.org/10.1016/j.lithos.2012.06.010.
Nutman, A.P., Bennett, V.C., Friend, C.R., Polat, A., Hoffmann, E., Kranendonk, M.V., 2021. Fifty years of the Eoarchean and the case for evolving uniformitarianism. Precambr. Res. 367 (106), 442. https://doi.org/10.1016/j.precamres.2021.106442.
Palin, R., Weller, O., Waters, D., Dyck, B., 2016. Quantifying geological uncertainty in metamorphic phase equilibria modeling; a Monte Carlo assessment and implications for tectonic interpretations. Geosci. Front. 7, 591–607. https://doi.org/10.1016/j.gsf.2015.08.005.
Palin, R., Reuber, G., White, R., Kaus, B., Weller, O., 2017. Subduction metamorphism in the Himalayan ultrahigh-pressure Tso Morari massif: An integrated geodynamic and petrological modelling approac. Earth Planet. Sci. Lett. 467 (108), 119. https://doi.org/10.1016/j.epsl.2017.03.029.
Palin, R., Santosh, M., Cao, W., Li, S., Hernández-Uribee, D., Parsons, A., 2020. Secular change and the onset of plate tectonics on Earth. Earth-Sci. Rev. 207 (103), 172. https://doi.org/10.1016/j.earscirev.2020.103172.
Park, R., Tarney, J., 1987. The Lewisian complex: a typical Precambrian high-grade terrain? Geological Society, London, Special Publication 27, 13–25. https://doi.org/10.1144/GSL.SP.1987.027.01.03.
Peach, B., Horne, J., Gunn, W., Clough, C., Hinxman, L., & Cadell, H. (1907), The geological structure of the North West Highlands of Scotland, Memoirs of the Geological Survey of Great Britain.
Percival, J., Skulski, T., Sanborn-Barrie, M., Stott, G., Leclair, A., Corkery, M., & Boily, M. (2012), Geology and Tectonic Evolution of the Superior Province, Canada, in Tectonic Styles in Canada: The LITHOPROBE Perspective, edited by J. Percival, F. Cook, & R. Clowes, pp. 321–378, Geological Association of Canada, Special Paper 49.

Piccolo, A., Palin, R., & B.J.P. Kaus, R.W. (2019), Generation of Earth's Early Continents From a Relatively Cool Archean Mantle, Geochemistry, Geophysics, Geosystems, 20, 1679–1697, doi:https://doi.org/10.1029/2018GC008079.
Pitzer, K., Sterner, S., 1994. Equations of state valid continuously from zero to extreme pressures for H2O and CO2. J. Chem. Phys. 101, 3111–3116. https://doi.org/10.1063/1.467624.
Polat, Ali, Wang, Lu, Appel, Peter, 2015. A review of structural patterns and melting processes in the Archean craton of West Greenland: Evidence for crustal growth at convergent plate margins as opposed to non-uniformitarian models. Tectonophysics 662, 67–94. https://doi.org/10.1016/j.tecto.2015.04.006.
Powell, R., Holland, T., 2008. On thermobarometry. J. Metamorph. Geol. 26, 155–179. https://doi.org/10.1111/j.1525-1314.2007.00756.x9.
Rollinson, H., 2012. Geochemical constraints on the composition of Archaean lower continental crust: Partial melting in the Lewisian granulites. Earth Planet. Sci. Lett. 351–352, 1–12. https://doi.org/10.1016/j.epsl.2012.07.018.
Roman, Alberto, Arndt, Nicholas, 2020. Differentiated Archean oceanic crust: Its thermal structure, mechanical stability and a test of the sagduction hypothesis. Geochim. et Cosmochim. Acta 278, 65–77. https://doi.org/10.1016/j.gca.2019.07.009.
Rutter, E., Brodie, K., 2004. Experimental grain size-sensitive flow of hot-pressed Brazilian quartz aggregates. J. Struct. Geol. 26, 2011–2023. https://doi.org/10.1016/j.jsg.2004.04.006.
Rybacki, E., Dresen, G., 2004. Deformation mechanism maps for feldspar rocks. Tectonophysics 382, 173–187. https://doi.org/10.1016/j.tecto.2004.01.006.
Rybacki, E., Gottschalk, M., Wirth, R., Dresen, G., 2006. Influence of water fugacity and activation volume on the flow properties of fine-grained anorthite aggregates, Journal of Geophysical Research, 111. B 03, 203. https://doi.org/10.1029/2005JB003663.
Sharp, D., 1984. An Overview of Rayleigh-Taylor Instability. Physica 12D, 3–18.
Sheraton, J., Skinner, A., Tarney, J., 1973. In: Park, R., Tarney, J. (Eds.), The geochemistry of the Scourian gneisses of the Assynt district, in The Early Precambrian Rocks of Scotland and Related Rocks of Greenland. University of Keele, pp. 13–30.
Shinevar, W., Behn, M., Hirth, G., 2015. Compositional dependence of lower crustal viscosity. Geophys. Res. Lett. 42, 8333–8340. https://doi.org/10.1002/2015GL065459.
Sills, J., 1981. Geochemical studies of the Lewisian Complex of the western Assynt region, NW Scotland. Ph.D. thesis. University of Leicester.
Sills, J., 1982. The retrogression of ultramafic granulites from the Scourian of NW Scotland. Mineral. Mag. 46, 55–61. https://doi.org/10.1180/minmag.1982.046.338.10.
Sills, J., 1983. Mineralogical changes occurring during the retrogression of Archaean gneisses from the Lewisian complex of NW Scotland. Lithos 16, 113–124. https://doi.org/10.1016/0024-4937(83)90009-9.
Sizova, E., Gerya, T., Stüwea, K., Brown, M., 2015. Generation of felsic crust in the Archean: A geodynamic modeling perspective. Precambr. Res. 271, 198–224. https://doi.org/10.1016/j.precamres.2015.10.005.
Sizova, E., Gerya, T., Brown, M., Stüwea, K., 2018. What drives metamorphism in early Archean greenstone belts? Insights from numerical modeling, Tectonophysics 746, 587–601. https://doi.org/10.1016/j.tecto.2017.07.020.
Sotiriou, Paul, Polat, Ali, Windley, Brian, Kusky, Timothy, 2022. Temporal variations in the incompatible trace element systematics of Archean volcanic rocks: Implications for tectonic processes in the early Earth. Precamb. Res. 368, 106487 https://doi.org/10.1016/j.precamres.2021.106487.
Sutton, J., Watson, J., 1951. The pre-Torridonian metamorphic history of the Loch Torridon and Scourie areas in the NW highlands and its bearing on the chronological classification of the Lewisian. J. Geol. Soc. 106, 241–308. https://doi.org/10.1144/GSL.JGS.1950.106.01-04.16.
Taylor, R.J.M., Johnson, T., Clark, C., Harrison, R., 2020. Persistence of melt-bearing Archean lower crust for >200 m.y.–An example from the Lewisian Complex, northwest Scotland. Geology 48, 221–225. https://doi.org/10.1130/G46834.1.
Taylor, T.D., Acrivos, A., 1964. On the deformation and drag of a falling viscous drop at low Reynolds number. J. Fluid Mech. 18, 466–576. https://doi.org/10.1017/S0022112064000349.
van Haaften, W., White, S., 1998. Evidence for multiphase deformation in the Archean basal Warrawoona Group in the Marble Bar area. East Pilbara, Western Australia, Precambrian Research 88, 53–66. https://doi.org/10.1016/S0301-9268(97)00063-6.
van Kranendonk, M., 2021. Gliding and overthrust nappe tectonics of the Barberton Greenstone Belt revisited: A review of deformation styles and processes. S. Afr. J. Geol. 124, 181–210 doi:https://doi.org/10.25131/sajg.124.0017.
van Kranendonk, M.J., Collins, W., Hickman, A., J.Pawley, M., 2004. Critical tests of vertical vs. horizontal tectonic models for the Archaean East Pilbara Granite-Greenstone Terrane. Pilbara Craton, Western Australia, Precambrian Research 131, 173–211. https://doi.org/10.1016/j.precamres.2003.12.015.
van Kranendonk, M.J., Kroner, A., Hoffmann, J., Nagel, T., Anhaeusser, C., 2014. Just another drip: Re-analysis of a proposed Mesoarchean suture from the Barberton Mountain Land. South Africa, Precambrian Research 254, 19–35. https://doi.org/10.1016/j.precamres.2014.07.022.
van Kranendonk, M.J., Smithies, M., Griffin, W., Huston, D., Hickman, A., Champion, D., Anhaeusser, C., & Pirajno, F. (2015), Making it thick: a volcanic plateau origin of Palaeoarchean continental lithosphere of the Pilbara and Kaapvaal cratons, in Continent Formation Through Time, edited by N.M.W. Roberts, M. van Kranendonk, S. Parman, S. Shirey, & P.D. Clift, pp. 83–111, Geological Society of London, Special Publications, doi: 10.1144/SP389.12.
Watkins, J., Clemens, J., Treloar, P., 2007. Archaean TTGs as sources of younger granitic magmas: Melting of sodic metatonalites at 0.6—1.2 GPa. Contrib. Miner. Petrol. 154, 91–110. https://doi.org/10.1007/s00410-007-0181-0.
Weller, O., St-Onge, M., Searle, M., Rayner, N., Waters, D., Chung, S., Palin, R., Lee, Y., Xu, X., 2013. Quantifying Barrovian metamorphism in the Danba Structural Culmination of eastern Tibet. J. Metamorph. Geol. 13, 909–935. https://doi.org/10.1111/jmg.12050.
Weller, O.M., Copley, A., Miller, W.G.R., Palin, R.M., Dyck, B.J., 2019. The relationship between mantle potential temperature and oceanic lithosphere buoyancy. Earth and Planetary Science Letters 518, 86–99. https://doi.org/10.1016/j.epsl.2019.05.005.
White, R., Powell, R., 2002. Melt loss and the preservation of granulite facies mineral assemblages. J. Metamorph. Geol. 20, 621–632. https://doi.org/10.1046/j.1525-1314.2002.00206_20_7.x.
White, R., Palin, R., Green, E., 2016. High-grade metamorphism and partial melting in Archean composite grey gneiss complexes. J. Metamorph. Geol. 35, 181–195. https://doi.org/10.1111/jmg.12227.
Whitehouse, M., & Kemp, A. (2010), On the difficulty of assigning crustal residence, magmatic protolith and metamorphic ages to Lewisian granulites: constraints from combined in situ U-Pb and Lu–Hf isotopes, in Continental Tectonics and Mountain Building: The Legacy of Peach and Horne, edited by R. Law, R. Butler, R. Holdsworth, M. Krabbendam, & R. Strachan, pp. 81–111, Geological Society, London, Special Publications, doi: 10.1144/SP335.5.
Whitney, D., Evans, B., 2010. Abbreviations for names of rock-forming minerals. Am. Mineral. 95, 185–187. https://doi.org/10.2138/am.2010.3371.
Wiemer, D., Schrank, C., Murphy, D., Wenham, L., Allen, C., 2018. Earth's oldest stable crust in the Pilbara Craton formed by cyclic gravitational overturns. Nat. Geosci. 11, 357–361. https://doi.org/10.1038/s41561-018-0105-9.
Windley, B., Bridgwater, D., 1973. The evolution of Archaean low and high grade terrains. In: Glover, J. (Ed.), The Archaean rocks. Australia, Special Publications, Geological Society, pp. 33–46.
Windley, B., Kusky, T., Polat, A., 2021. Onset of plate tectonics by the early Archean. Precambr. Res. 352 (105), 980. https://doi.org/10.1016/j.precamres.2020.105980.
Zirkler, A., Johnson, T., White, R., Zack, T., 2012. Polymetamorphism in the mainland Lewisian complex, NW Scotland – phase equilibria and geochronological constraints from the Cnoc an t'Sidhean suite. J. Metamorph. Geol. 30, 865–885. https://doi.org/10.1111/j.1525-1314.2012.01003.x.